

A Near Surface Temperature Model of Arrokoth

ORKAN M. UMURHAN ^{1,2,3,*} WILLIAM M. GRUNDY ^{4,*} MICHAEL K. BIRD ^{5,6,†} ROSS BEYER ^{1,2,*}
JAMES T. KEANE ^{7,†} IVAN R. LINSOTT ^{8,†} SAMUEL BIRCH ⁹ CARVER BIERSON ^{10,†} LESLIE A. YOUNG ^{11,*}
S. ALAN STERN ^{11,‡} CAREY M. LISSE ^{12,†} CARLY J.A. HOWETT ^{11,*} SILVIA PROTOPAPA ^{11,*}
JOHN R. SPENCER ^{13,*} RICHARD P. BINZEL ^{9,*} WILLIAM B. MCKINNON ^{14,*} TOD R. LAUER ^{15,*}
HAROLD A. WEAVER ^{16,*} CATHERINE B. OLKIN ^{13,*} KELSI N. SINGER ^{13,*} ANNE J. VERBISCHER ^{17,*} AND
ALEX H. PARKER ^{13,*}

¹SETI Institute, 189 Bernardo Way, Mountain View, CA 94043, U.S.A.

²NASA Ames Research Center; Mail Stop 245-3, Moffett Field, CA 94035, USA

³Cornell Center for Astrophysics and Planetary Sciences, Cornell University, Ithaca, NY, USA

⁴Lowell Observatory, 1400 W. Mars Hill Road, Flagstaff, AZ 86001, USA

⁵Argelander-Institut für Astronomie, Universität Bonn, 53121 Bonn, Germany.

⁶Rheinisches Institut für Umweltforschung, Universität zu Köln, 50931 Cologne, Germany.

⁷Jet Propulsion Laboratory, California Institute of Technology, Pasadena, CA 91125, USA

⁸Stanford University, Stanford, CA 94305, USA

⁹Department of Earth, Atmospheric and Planetary Science, Massachusetts Institute of Technology, Cambridge, MA 02139

¹⁰School of Earth and Space Exploration, Arizona State University, Tempe, AZ 85287, USA

¹¹Southwest Research Institute, 1050 Walnut Street, Suite 300, Boulder, CO 80302, USA

¹²Space Exploration Sector, Johns Hopkins University Applied Physics Laboratory, 11100 Johns Hopkins Rd, Laurel, MD 20723, USA

¹³Division of Space Science and Engineering, Southwest Research Institute, Boulder, CO 80302, USA

¹⁴Department of Earth and Planetary Sciences and McDonnell Center for the Space Sciences, Washington University, St. Louis, MO 63130, USA

¹⁵National Optical- Infrared Astronomy Research Laboratory, National Science Foundation, Tucson, AZ 85726, USA

¹⁶Johns Hopkins University Applied Physics Laboratory, Laurel, MD 20723, USA

¹⁷Department of Astronomy, University of Virginia, Charlottesville, VA 22904, USA

(Received February 23, 2022)

ABSTRACT

A near surface thermal model for Arrokoth is developed based on the recently released 10⁵ facet model of the body. This thermal solution takes into account Arrokoth's surface re-radiation back onto itself. The solution method exploits Arrokoth's periodic orbital character to develop a thermal response using a time-asymptotic solution method, which involves a Fourier transform solution of the heat equation, an approach recently used by others. We display detailed thermal solutions assuming that Arrokoth's near surface material's thermal inertia $\mathcal{I} = 2.5 \text{ W/m}^{-2}\text{K}^{-1}\text{s}^{1/2}$. We predict that at New Horizons' encounter with Arrokoth its encounter hemisphere surface temperatures were $\sim 57\text{-}59 \text{ K}$ in its polar regions, $30\text{-}40 \text{ K}$ on its equatorial zones, and $11\text{-}13 \text{ K}$ for its winter hemisphere. Arrokoth's orbitally averaged temperatures are around $30\text{-}35 \text{ K}$ in its polar regions, and closer to 40 K near its equatorial zones. Thermal reradiation from the surrounding surface amounts to less than 5% of the total energy budget, while the total energy ensconced into and exhumed out Arrokoth's interior via thermal conduction over one orbit is about 0.5% of the total energy budget. As a generalized application of this thermal modeling together with other KBO origins considerations, we favor the interpretation that New Horizons' REX instrument's $29 \pm 5 \text{ K}$ brightness temperature measurement is consistent with Arrokoth's near surface material's being made of sub-to-few mm sized tholin-coated amorphous H₂O ice grains with $1 \text{ W/m}^{-2}\text{K}^{-1}\text{s}^{1/2} < \mathcal{I} < 10\text{-}20 \text{ W/m}^{-2}\text{K}^{-1}\text{s}^{1/2}$, and which are characterized by an X-band emissivity in the range 0.9 and 1.

Keywords: Classical Kuiper belt objects(250) — Small Solar System bodies(1469) — Natural satellite surfaces(2208) — Computational Methods(1965)

1. INTRODUCTION

The bilobate object Arrokoth (discovered by [Buie et al. 2020](#), as 2014 MU₆₉) is a flattened ($\sim 10\text{km} \times 20\text{km} \times 30\text{km}$), 15.9 hour rotating, high obliquity ($\sim 99^\circ$) Kuiper Belt Object (KBO) encountered by the New Horizons spacecraft on January 1, 2019 (JD 2458485, [Stern et al. 2019](#)). Owing to its relatively low eccentricity and inclination ($e = 0.03$, $i = 2.4^\circ$, respectively) and its location in the Kuiper Belt ($a = 44.58\text{AU}$, and orbital frequency $\omega = 6.69 \times 10^{-10}\text{s}^{-1}$), it falls into the class of so-called cold classical KBOs (or CCKBO, for short) and, as such, is considered a Kuiper Belt planetesimal, being perhaps one of the oldest and relatively unprocessed relics of the solar system’s formation era ([McKinnon et al. 2020](#)). Its surface, with low mean hemispherical albedo ($A \approx 0.063$, [Stern et al. 2019](#); [Hofgartner et al. 2021](#)), exhibits a relatively featureless H₂O-free infrared spectrum save for the possible presence of surface methanol ice (CH₃OH) observed in absorption ([Grundy et al. 2020](#)). Arrokoth does not appear to exhibit signs of harboring any volatile species ([Lisse et al. 2021](#)).

Furthermore, thermal X-band emission of Arrokoth (4.2-cm wavelength, 7.2 GHz) was observed by New Horizons’ Radio Science Experiment (REX) in both its face on approach (low-phase angle) and look-back (high-phase angle) perspective. Fig.1 shows a visual view of Arrokoth a few minutes prior to the look-back phase REX scan. Analysis of the winter night side thermal emission is consistent with a mean observed brightness temperature $T_{b,\text{obs}} = 29 \pm 5\text{ K}$ ([Grundy et al. 2020](#), also [Bird et al. 2022](#), this volume). Although New Horizons was unable to directly measure Arrokoth’s thermal inertia, based on other observed properties of CCKBOs it is assumed to lie somewhere between 1-10 tiu ([Lellouch et al. 2013](#); [Müller et al. 2020](#), also 1 tiu = $1\text{ Wm}^{-2}\text{K}^{-1}\text{ s}^{1/2}$), indicative of highly insulating material – at least for surface thicknesses corresponding to diurnal skin depths ($\sim 1\text{-}2\text{ mm}$). For such a thermal inertia value applied to Arrokoth, together with an assumed low heat capacity material, predicts a seasonal (i.e., one orbit timescale = 297.6yr) thermal skin depth of about 1 m ([Grundy et al. 2020](#)). Geomorphological analysis of Arrokoth’s approach hemisphere seem to exhibit rel-

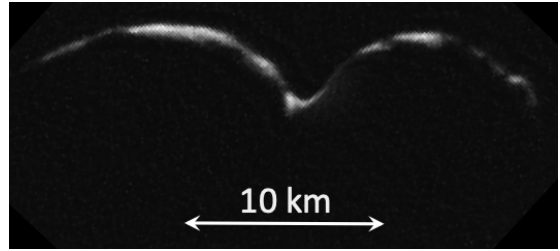


Figure 1. View of Arrokoth (CA07) taken by the LORRI camera on its departure trajectory approximately 10 minutes prior to the second REX scan ([Grundy et al. 2020](#)). The lit crescent seen here would have appeared somewhat diminished during the actual REX scan ($\sim 10^\circ$ shift in viewing geometry).

atively bright surface units, especially in regions close to Arrokoth’s neck ([Spencer et al. 2020](#)). What relationship, if any, do these features have with the kinds of surface temperatures likely on Arrokoth’s surface? Furthermore, how does Arrokoth’s relatively bright neck region correlate to both the seasonal cycle of received insolation and resulting surface temperatures there? Lastly, can the REX brightness temperature measurement be connected to and properly reconciled with a realistic temperature model for Arrokoth?

It is thus important to generate a thermophysical temperature map of Arrokoth to help address these questions. Stereo pair images taken by New Horizons’ Long-Range Reconnaissance Imager (LORRI) [Spencer et al. \(2020\)](#) have been used to produce several cartographic data products including both a global shape model and a relatively detailed topographic map of Arrokoth’s closest approach day-side hemisphere. Together with this $\sim 10^5$ element shape model and Arrokoth’s known orbital elements, Arrokoth’s instantaneous distance from the Sun (r), as well as its subsolar latitude along every point along its orbit are also known ([Porter et al. 2018](#)).

Although New Horizons did not attempt a direct gravity measurement of Arrokoth, an estimate for the body’s bulk mass density may be made by applying the gravitational slope analysis of [Richardson & Bowling \(2014\)](#) by using the shape/topographic model of [Spencer et al. \(2020\)](#), which suggests that the body’s mean density may be as little as $\rho = 150\text{ kg/m}^3$ and as high as $\rho = 650\text{ kg/m}^3$ ([McKinnon et al. 2020](#); [Keane et al. 2020](#), [Keane et al. 2021](#)). For our purposes we will adopt a nominal value of $\rho = 250\text{ kg/m}^3$, also see detailed dis-

* New Horizons Science Team, Co-Investigator

† New Horizons Science Team, Science Affiliate

‡ New Horizons Science Team, Principal Investigator

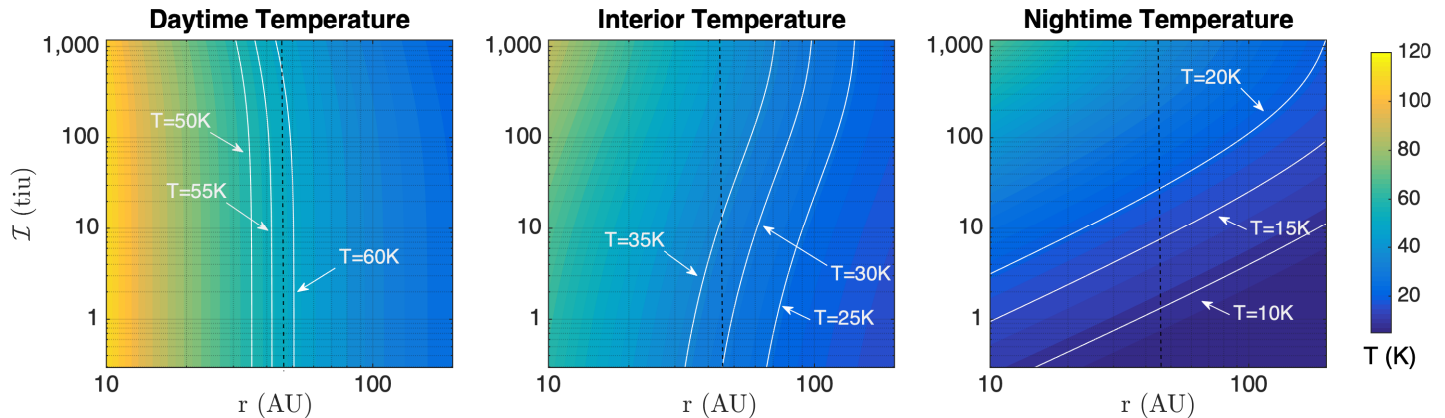


Figure 2. Predicted temperatures based on the simple theory of Section 2. Each panel shows the predicted temperatures as a function of distance from Sun (r) and thermal inertia (\mathcal{I}). All models assume $A = 0.06$ and $\varepsilon = 0.9$. The background flux consists entirely of the microwave background. The panels depict (left panel) predicted summer season temperatures $T_{s,s}$, (middle panel) predicted interior temperatures T_{int} , and (right panel) predicted winter season temperatures $T_{s,w}$. The vertical hatched lines show the location of 44 AU and various iso-temperature lines of interest are shown with white curves.

discussion in Keane et al. (2021).¹ Fully compacted KBOs have typical densities of about $\sim 1500\text{kg/m}^3$ (e.g., see compilation found in Bierson & Nimmo 2019), thus if Arrokoth is made of the same stuff, then its bulk porosity p reasonably falls somewhere within the range of 0.6 to 0.85. Also, for reference we note the only direct measured density of a comet nucleus is that for 67P/Churyumov-Gerasimenko at around 533 kg/m^3 (Pätzold et al. 2016). However we do note that Arrokoth’s topmost layers – on the scale of a few seasonal thermal skin depths – may have mean densities that deviate from the bulk average either due to compaction by impacts over geologic time or due to porosity increase due to volatile sublimation during the body’s earliest times after formation. However, compaction appears to be less likely owing to the paucity of impact craters on Arrokoth (Stern et al. 2019; Spencer et al. 2020; McKinnon et al. 2020).

Another key input is the unconstrained value of Arrokoth’s surface ice’s heat capacity at constant pressure, C_p , a quantity not directly measured by New Horizons’ flyby of the body. For the thermal solutions developed

in Grundy et al. (2020), a value $C_p = 350\text{ J/K/kg}$ was adopted based on estimates for cold H_2O Ih ice where $C_p \approx 180\text{ J/K/kg}$ (Castillo-Rogez et al. 2012), and similar to adopted empirical forms like that found in Klinger (1980) and Shulman (2004). The nearly doubled value can be rationalized on the argument that organic impurities and/or the presence of methanol in the matrix would substantially boost the ice complex’s heat capacity. This point is examined further in Section 6.1.3.

With these input ingredients, together with some assumptions regarding the surface thermal inertias, one may construct a current era temperature map of Arrokoth’s surface, which is a vast improvement over the one presented in Umurhan et al. (2019) and Grundy et al. (2020), which was based on a relatively coarse ~ 2000 element shape model.

The main purpose of this study is detailing a general framework for generating temperature models of Arrokoth based on this 10^5 facet shape model. Although we do not directly address the questions posed earlier in this introduction – especially connecting the predicted temperature profiles to the departure phase REX *brightness temperature* measurement (see companion study by Bird et al. 2022) – the temperature solutions developed here will be employable toward answering all of them in future studies.

The rest of this study is structured as following: Section 2 presents a simple thermal solution in order to ground our intuition as to what to expect. Section 3 describes the thermal solution method, which includes a discussion of the shape model, the self-obscurtion analysis of the shape model, a detailed description of how insolation is calculated over the course of one orbit, and finally a description of the Fourier transform based

¹ There are no direct constraints on Arrokoth’s density. The quoted values are based on an empirical trend inferred from the observations of other small airless bodies of the solar system. For a body of given shape and rotation, the distribution of topographic slopes corresponds to maximum stability, i.e., the statistical slope distribution is furthest removed from the material’s angle of repose (Richardson & Bowling 2014; Richardson et al. 2019). McKinnon et al. (2020) finds this state of maximum stability by tuning the mean density to around 235 kg/m^3 with the quoted 1σ error range. We are cautioned that these are only indirect estimates based on geophysical inference and analogy to comets and asteroids.

solution to the thermal diffusion equation. Section 4 surveys our results in which we break up our discussion into encounter day thermal properties and orbitally averaged features. In Section 5 we develop the analysis framework that connecting the observed brightness temperature to the thermal solutions developed here. Section 6 discusses aspects of our results together with several speculations including a theoretical discussion that regarding the nature of Arrokoth’s thermal inertia, as well as a few caveats. Section 7 concludes with a short summary. The various appendices contain details of the methods used for our thermal solutions as well as details of the radiative transfer modeling employed here.

2. A SIMPLIFIED PHYSICS-BASED EMPIRICAL THERMAL MODEL

To guide our intuition we present a simple thermal model to ground expectations. The model is one dimensional and is intended to crudely represent a thermal response of a facet over the course of one orbit with frequency ω . Its construction is ‘physics-based’ in the sense that it is a pared-down casting of the more complete thermophysical model described in the next section.

The model is constructed in two parts and interpreted in terms of “winter” and “summer” time exposure given Arrokoth’s high obliquity, relatively flattened shape, and consequent extreme polar winters and summers. Our view of this is guided by the observation that at high summer the daylit side of Arrokoth is close to a flat slab baking under the Sun, while at high winter the same slab is in total darkness while at the equinoxes, Arrokoth’s surfaces are only tangentially illuminated.

The first part describes the temperature profile resulting on the surface and interior while the face is illuminated by the Sun with absorbed flux $f_{\text{eff}} = (1 - A)f_{\odot}$, in which f_{\odot} is the peak summer solstice illumination flux, and where A is the material albedo. If r is the body’s orbital radius (in AU) with $f_{\text{SC}} = 1366\text{W/m}^2$ (defined as the solar constant), then the peak solar irradiance is $f_{\odot} = f_{\text{SC}}/r^2$. In this statement of the problem $\omega = \omega_{\oplus} r^{-3/2}$ where $\omega_{\oplus} = 1.99 \times 10^{-7} \text{ s}^{-1}$. The summer season’s subsurface temperature model, $T_s(z)$, is

$$T_s = T_{\text{int}} + (T_{s,s} - T_{\text{int}}) e^{kz}, \quad (1)$$

in which $T_{s,s}$ and T_{int} are the summer season surface temperature and deep interior temperature (respectively). The thermal skin depth scale (ℓ) is given by $2\pi/k$ where

$$k \equiv \sqrt{\rho C_p \omega / K}, \quad (2)$$

with K being the effective material conductivity, ρ the ice mass density, C_p the ice specific heat at constant

pressure. We will often refer to the effective thermal inertia of the medium, defined as

$$\mathcal{I} \equiv \sqrt{K\rho C_p}. \quad (3)$$

The above postulated energy balance at the surface during the day entails

$$\underbrace{(1 - A)f_{\odot} + f_{\text{bg}}}_{\text{received energy flux}} = \underbrace{Kk(T_{s,s} - T_{\text{int}})}_{\text{conducted thermal flux}} + \underbrace{\epsilon_{\text{ir}}\sigma T_{s,s}^4}_{\text{radiative losses}}, \quad (4)$$

in which ϵ_{ir} is the material’s thermal infrared emissivity, σ is the Stefan-Boltzmann constant and f_{bg} represents a constant background illumination source.

The second part of the model describes the temperature response during the winter season, in which the surface is illuminated only by the background radiation field f_{bg} , which we here adopt to be just the cosmic microwave background, i.e., $f_{\text{bg}} \approx f_{\text{cmb}} \approx 3.15 \times 10^{-6}\text{W/m}^2$, corresponding to $T_{\text{cmb}} = 2.725\text{K}$. The corresponding winter season temperature solution is $T_w(z)$ where

$$T_w = T_{\text{int}} + (T_{s,w} - T_{\text{int}}) e^{kz}, \quad (5)$$

where $T_{s,w}$ is the night time surface temperature. The corresponding surface energy balance, analogous to Eq. (4), is given by

$$f_{\text{bg}} = Kk(T_{s,w} - T_{\text{int}}) + \epsilon_{\text{ir}}\sigma T_{s,w}^4. \quad (6)$$

These coupled sets of equations are supplemented by an expression linking the winter and summer season solutions. For this we impose the condition that all of the energy conducted into the surface during summer returns to the surface in winter. Therefore we have

$$Kk(T_{s,w} - T_{\text{int}}) = -Kk(T_{s,s} - T_{\text{int}}) \quad (7)$$

Thus, Eqs. (4,6,7) constitute a complete set of (algebraic) equations for the three unknowns $T_{s,w}$, $T_{s,s}$ and T_{int} . From Eq. (7) it immediately follows that the interior temperature is simply the average of the day and night side temperatures, i.e., $T_{\text{int}} = (T_{s,s} + T_{s,w})/2$. The solution curves are governed by two non-dimensional numbers. The first of these is η , given by

$$\eta \equiv \left(\frac{f_{\text{bg}}}{(1 - A)f_{\odot} + f_{\text{bg}}} \right)^{1/4}, \quad (8)$$

where η is the ratio of the surface flux temperatures between the night and day side. From this one may define averaged summertime and wintertime flux temperatures, \bar{T}_s and \bar{T}_w (respectively), in which

$$\bar{T}_s \equiv \left(\frac{(1 - A)f_{\odot} + f_{\text{bg}}}{\epsilon_{\text{ir}}\sigma} \right)^{1/4}, \quad \bar{T}_w \equiv \left(\frac{f_{\text{bg}}}{\epsilon_{\text{ir}}\sigma} \right)^{1/4}. \quad (9)$$

The second non-dimensional parameter Γ is the thermal parameter introduced by Spencer, which we hereafter refer to as the Spencer Number, and is defined here as

$$\Gamma \equiv \frac{(\rho C_p K \omega)^{1/2} \bar{T}_s}{(1-A)f_\odot + f_{bg}} \rightarrow \frac{(\rho C_p K \omega)^{1/2} (\epsilon_{ir} \sigma)^{-1/4}}{[(1-A)f_\odot + f_{bg}]^{3/4}}, \quad (10)$$

estimating the relative contribution of downward directed thermal flux and radiative losses to space.² The simplified non-dimensional equations that must be simultaneously solved are

$$1 - \frac{1}{2}\Gamma(\theta_s - \eta\theta_w) - \theta_s^4 = 0, \quad (11)$$

$$1 + \frac{1}{2}\Gamma\eta^{-4}(\theta_s - \eta\theta_w) - \theta_w^4 = 0, \quad (12)$$

where $\theta_s \equiv T_{s,s}/\bar{T}_s$ and $\theta_w \equiv T_{s,w}/\bar{T}_w$. We observe that holding all input quantities constant but only varying the orbital radius, so long as $(1-A)f_\odot \gg f_{bg}$ it follows that $\Gamma \sim r^{3/4}$, which says that the importance of surface thermal conduction increases as an object like Arrokoth moves further away from the Sun.

In Figure 2, we plot the predicted day and night side temperatures, as well as the predicted deep interior temperature, for conditions representative for those of Arrokoth, wherein we adopt $\epsilon_{ir} = 0.9$, $A = 0.06$, $\rho = 250\text{kg/m}^3$, and $C_p \approx 350\text{ J/K/kg}$. For the sake of academic completeness, we show what the predicted values of these varied temperature quantities for various radial positions ($10\text{ AU} < r < 150\text{ AU}$) and thermal inertias $0.1\text{ tiu} < \mathcal{I} < 100\text{ tiu}$, while keeping in mind that the likely values of Arrokoth's \mathcal{I} is in the range of 1-10 tiu, together with a nominal value of $r = 44\text{ AU}$. This relatively uncomplicated physics-based empirical model predicts a range of averaged daytime surface temperatures in the vicinity of 55-60 K, deep interior temperatures between 34 K and 38 K, with typical averaged nighttime temperatures in the range of 10-20 K. The winter side temperature reflects the subsurface heat flux returning to the surface. In this respect it represents the balance between the emerging thermal conductive flux and blackbody radiative losses of Eq. (6). We will revisit these predictions in light of the full calculation we develop in the next two sections.

3. FULL BODY THERMAL MODEL: FORMULATION

The simple equilibrium model presented in the previous section is useful for understanding the basic thermophysics of Arrokoth, but it assumes a slab-like surface

² This non-dimensional parameter is often denoted in the literature by the symbol “ Θ ”, but we use Γ here because Θ is used elsewhere in this manuscript to denote Fourier temperature components.

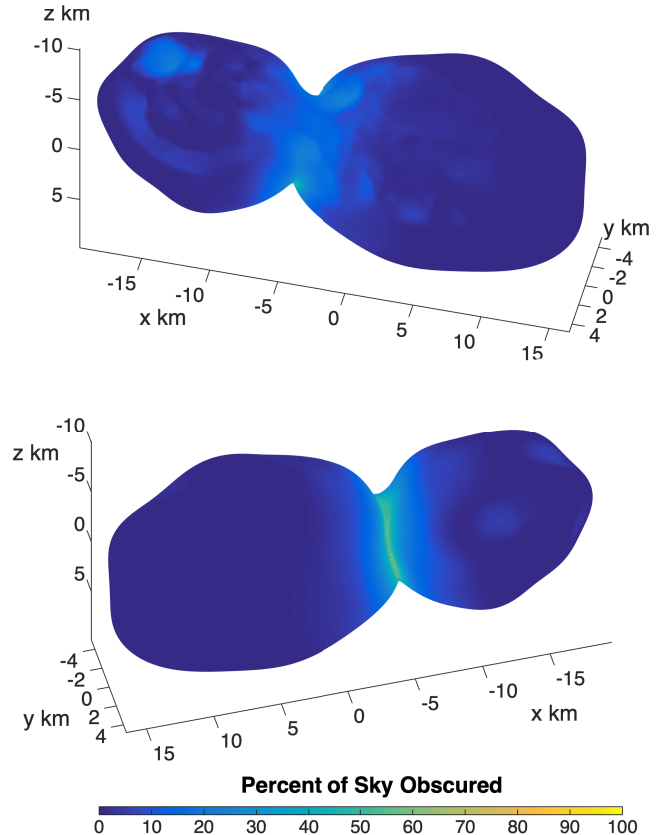


Figure 3. Percent of sky self-obscured of the 10^5 merged shape model. The views shown are approximately from the approach trajectory (CA03, top panel) and departure trajectory (CA07, bottom panel). This references discussions found in both Secs. 3.1-3.2, as well as Appendix A.

where each facet is only in simple radiative equilibrium with the sky, and does not see other parts of Arrokoth's warm surface. Here we enhance the modeling by including the detailed shape and illumination information gained by the New Horizons flyby of Arrokoth.

Given a body's shape model with a set of N facets labeled by “ i ” each of whose centers are given by the vector \mathbf{r}_i in the coordinate frame of the body's center of mass (see section 3.2 below), we solve for its temperature profile as a function of depth normal to the surface. This is justified on the assumption that the seasonal thermal skin depth ($\sim 1 - 2\text{m}$) is small compared to the horizontal scale of each facet ($\sim 50 - 100\text{m}$) and on the assumption there are no other heat sources or sinks deep in Arrokoth's interior after 4.56 Gyr of evolution (c.f., Lisse et al. 2021). We therefore define the variable $\Theta_i(z, t)$ to be the temperature in the z -direction underneath each facet i , where $z = 0$ is the surface. We furthermore identify $T_i(t) = \Theta_i(z = 0, t)$ as the sur-

Table 2. Various quantities and parameters, and their adopted values where appropriate.

Quantity	Value	Reference
Mass density of surface materials, ρ	150-650 kg/m ³	McKinnon et al. (2020); Keane et al. (2020)
Specific heat at constant pressure, C_p	350 J/K/kg	Castillo-Rogez et al. (2012) + Grundy et al. (2020)
Thermal inertia, \mathcal{I}	1-10 W/m ² /K/s ^{-1/2}	Lellouch et al. (2013)
Diurnal timescale thermal skin depth, ℓ_{day}	~ 1 mm	Grundy et al. (2020)
Arrokoth's semimajor axis, r	44.58 AU	Buie et al. (2020)
Orbital frequency of Arrokoth, ω	6.69×10^{-10} s ⁻¹ (298 yr orbit)	Porter et al. (2018)
Diurnal frequency of Arrokoth, ω_{d}	1.10×10^{-4} s ⁻¹ (15.9 hr day)	Buie et al. (2020)
Obliquity	99.1°	Spencer et al. (2020)
Mean hemispherical albedo, A	$\sim 0.063 \pm 0.015$	Hofgartner et al. (2021)
thermal infrared emissivity, ϵ_{ir}	~ 0.9	Grundy et al. (2020)

face temperature of facet i . For this initial study we assume the thermal conductivity to be independent of temperature, although the methods described here are generalizable to variable K . The temperature response therefore satisfies the linear heat equation

$$\rho C_p \partial_t \Theta_i = \partial_z (K \partial_z \Theta_i), \quad (13)$$

subject to boundary conditions, one of which is nonlinear. We assume that the deep interior of Arrokoth no longer has any active heat sources (an assumption likely not true during right after it was formed) and, as such, we assume the thermal flux goes to zero with large enough depth, i.e.,

$$\lim_{z \rightarrow -\infty} K \partial_z \Theta_i = 0. \quad (14)$$

The nonlinearities in this problem are expressed in the upper boundary condition, which is statement of the balance of received, emitted and interior transmitted energies, like embodied in the similar expressions utilized in the previous section, namely Eqs. (4,6). We do not consider the sublimation of volatile species given no observation of any gas emission. We furthermore assume the albedo is uniform across the surface. Thus at each facet surface we write

$$\epsilon_{\text{ir}} \sigma T_i^4 = (1 - A) f_{\odot, i} + f_{\text{bg}} + K \partial_z T_i + \int_{\partial S} \epsilon \sigma T_j^4 S_{ij} d\hat{s}_j, \quad (15)$$

where $K \partial_z T_i \equiv K \partial_z \Theta_i|_{z=0}$. We note that the received solar insolation on facet i , $f_{\odot, i}$, is time dependent (see sec. 3.3). The last term in the above expression represents the reradiated infrared radiation integrated over all facets j , with infinitesimal surface element $d\hat{s}_j$, that are visible to facet i . We assume that the infrared albedo is 0. The actual amount of reradiated radiation received at facet i is contained in the matrix S_{ij} , which includes information about the relative inclination angle between

each facet pair, inverse square law effects and other mitigating factors (see further below). We have assumed that a given facet only radiates infrared light, contained in the frequency integrated expression $\epsilon_{\text{ir}} \sigma T_j^4 S_{ij}$, with no contribution due to reflected light. This neglect is justified (see Sec. 5.3.1) on account of the relatively low value of A . A proper treatment of this contribution should be included in future analyses of Arrokoth.

Eqs. (13-15) constitute the nonlinear partial differential equations to be solved for every T_i and generating a solution over one orbital period. In the following subsections we provide a high-level view of the solution method we here employ. The methodology used here is described in part in the Supplemental Materials of Grundy et al. (2020) and were used to derive the solutions presented also in Umurhan et al. (2019).

3.1. The Shape Model

We use the merged shape model described in Spencer et al. (2020). That model consists of a closed three-dimensional best-fit shape derived from monoscopic images (Porter et al. 2019), upon which a topographic surface of the spin-pole negative face derived from stereogrammetry is fitted and merged (Beyer et al. 2019a). The model contains 107,506 facets, which have an average area of 0.013 km² (with a standard deviation of 0.006 km²), which corresponds to a typical facet diameter of about 100m – this being the highest resolution achieved during New Horizons closest approach. A flavor of the shape model is displayed in Fig. 3. The shape model is saved as a meshfile (.obj file format) and will be a part of a forthcoming New Horizons PDS Small Bodies Node (SBN) release³ scheduled for late 2021 (in preparation). Fig. 4 shows a Lucy-Richardson stacked deconvolved LORRI image of Arrokoth overlain with a single

³ https://pds-smallbodies.astro.umd.edu/data_sb/missions/newhorizons/index.shtml

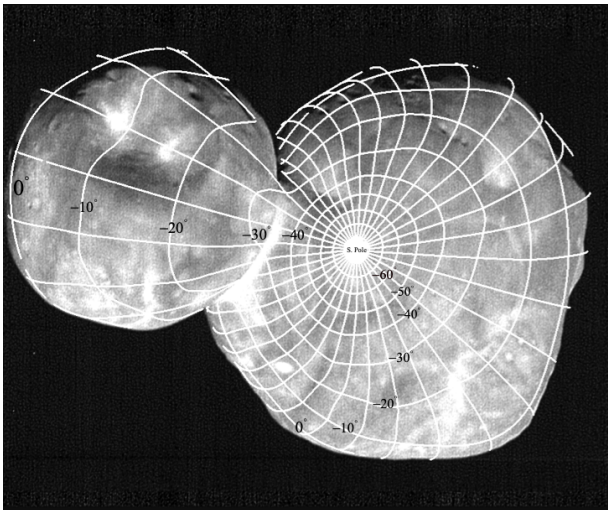


Figure 4. A Lucy-Richardson stacked deconvolved image from the LORRI CA06 sequence (images LOR_0408626328 through LOR_0408626336). A single longitude/latitude graticule centered on the spin-pole is overlaid. The negative-spin pole faced the Sun during the New Horizons flyby. Thus, this view corresponds to the “southern” hemisphere.

latitude-longitude graticule. Given Arrokoth’s $> 90^\circ$ obliquity, the approach view is from the “southern” hemisphere, i.e., those of the negative latitudes. Because of Arrokoth’s concave shape, a latitude-longitude coordinate representation is impractical for our purposes as it can lead to degeneracies (see also Keane et al, 2021). We typically refer to such conventions for qualitative discussion purposes only. For all of our calculations this work uses a Cartesian system centered on the body’s center of Fig. 4 (see Beyer et al. 2019b) .

3.2. Shape Analysis: S_{ij} and K_{ij}

A shape analysis here is concerned with assessing a “who-sees-who” network, identifying which facets j of a shape are visible to a given facet i . This information is then used to determine how much re-radiation is subsequently received. We have constructed our own shape analysis algorithm, which is detailed in Appendix A, that largely mirrors the approach and philosophy utilized in several similarly motivated examinations of other solar system bodies, e.g., like that used for the Moon (Gläser & Gläser 2019), 67P (Tosi et al. 2019), and asteroids (Rozitis & Green 2011). The shape and transfer model converts the continuous integral of Eq. (15) into a discrete matrix operation, i.e.,

$$\int_{\partial S} \epsilon_{\text{ir}} \sigma T_j^4 S_{ij} d\hat{s}_j \rightarrow \sum_{\forall j \text{ visible}} \epsilon \sigma T_j^4 K_{ij}, \quad (16)$$

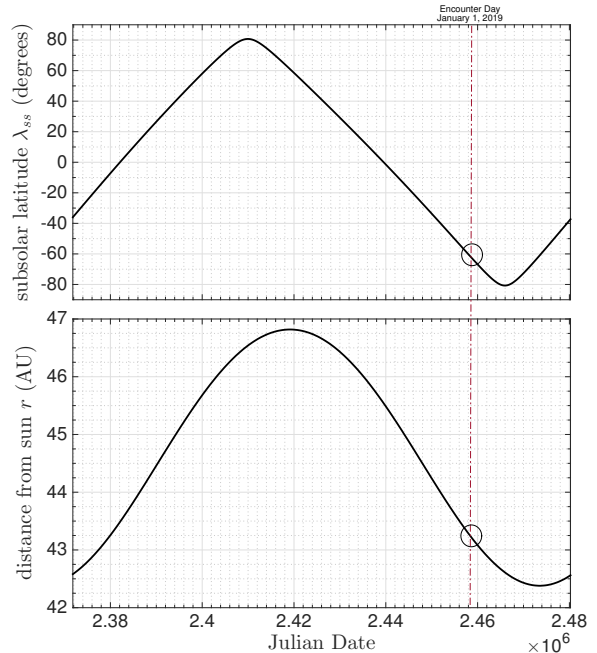


Figure 5. Subsolar latitude on Arrokoth (λ_{ss} , top panel) and its instantaneous distance from the Sun (r , bottom panel) over the course of one Arrokoth orbit and consistent with the body’s 99.1° obliquity. The encounter day properties are shown with a vertical hatched line. These are solutions based on the study found in Porter et al. (2018).

where K_{ij} contains knowledge of the “who-sees-who” network as well as the amount of radiative transfer communicated between element pairs.

3.3. Calculating Diurnal Averaged Insolation $f_{\odot,i}$

Because the rotation rate is so short compared to the orbital time, we calculate the diurnally averaged insolation received by each facet i . Figure 5 shows both Arrokoth’s subsolar latitude, $\lambda_{ss}(t)$, and its instantaneous distance from the Sun, $r(t)$ (in AU), over the course of one nearly 300 year orbit (Porter et al. 2018). The instantaneous flux of solar radiation crossing Arrokoth’s location is therefore $f_r \equiv f_{\text{sc}}/r^2$. With respect to the shape model described in the previous section, the direction of the Sun is given by the unit vector $\hat{\mathbf{n}}_{\text{sun}}$ whose individual components are

$$\begin{aligned} n_{x,\text{sun}} &= \cos \varphi \sin (\pi/2 - \lambda), \\ n_{y,\text{sun}} &= \sin \varphi \sin (\pi/2 - \lambda), \\ n_{z,\text{sun}} &= \cos (\pi/2 - \lambda), \end{aligned} \quad (17)$$

wherein φ is the longitude corresponding to peak illumination (“high noon”) on Arrokoth. Then with respect

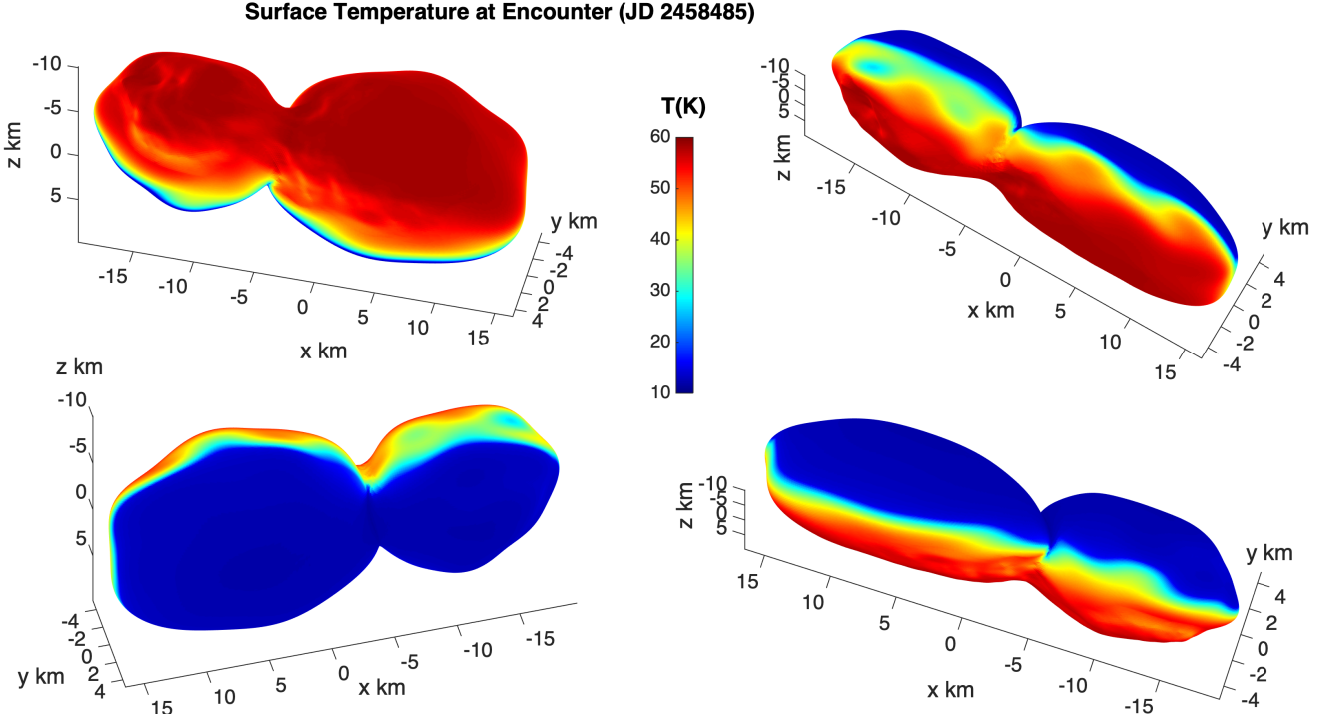


Figure 6. Predicted surface temperatures on encounter day (January 1, 2019) on the assumption $\mathcal{I} = 2.54$ tiu and $\varepsilon = 0.9$. The upper left shows a view of the body on approach while the lower left depicts the view of Arrokoth during the CA08 observation. The upper and lower right panels are the same model but rotated to emphasize the view of the equatorial regions.

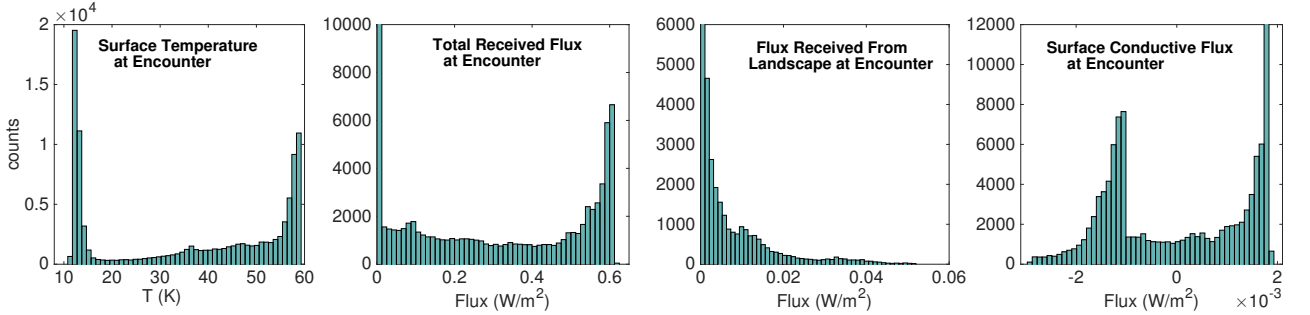


Figure 7. Histogram plots for various predicted quantities on encounter day (January 1, 2019). Model assumes $\mathcal{I} = 2.54$ tiu and $\varepsilon = 0.9$. Vertical axis corresponds to number of facets. Of the shown panels: (far left) Distribution of surface temperatures, (middle left) Total received flux, (middle right) flux received as reradiation from surrounding landscape and, (far right) surface conductive flux in which a negative value corresponds to surface directed flow of energy from the interior. In the last of these, note the trailing wing corresponding to the intense flux ring seen evident in Fig. 9.

to facet i with unit normal $\hat{\mathbf{n}}_i$, and where high noon occurs over longitude φ with subsolar latitude $\lambda \rightarrow \lambda_{ss}$, the local flux of solar radiation received at facet is

$$f_{\oplus,i}(\varphi, \lambda) = \begin{cases} 0, & \text{if ray blocked or } \hat{\mathbf{n}}_i \cdot \hat{\mathbf{n}}_{\text{sun}} < 0, \\ f_r \hat{\mathbf{n}}_i \cdot \hat{\mathbf{n}}_{\text{sun}}, & \text{otherwise.} \end{cases} \quad (18)$$

where the condition $\hat{\mathbf{n}}_i \cdot \hat{\mathbf{n}}_{\text{sun}} < 0$ means the Sun is below the horizon. Note that like the shape analysis de-

scribed in the previous section, we must execute ray-tracing routine to determine if other facets block the Sun's rays from reaching the given facet. While this can be extremely expensive, in practice we reduce the actual number of ray-tracing determinations by taking into account knowledge of the maximum landscape altitude angle β_i determined in the shape analysis: if the sun vector $\hat{\mathbf{n}}_{\text{sun}}$ points with an angle with respect to the local facet horizontal that exceeds the angle β_i , then

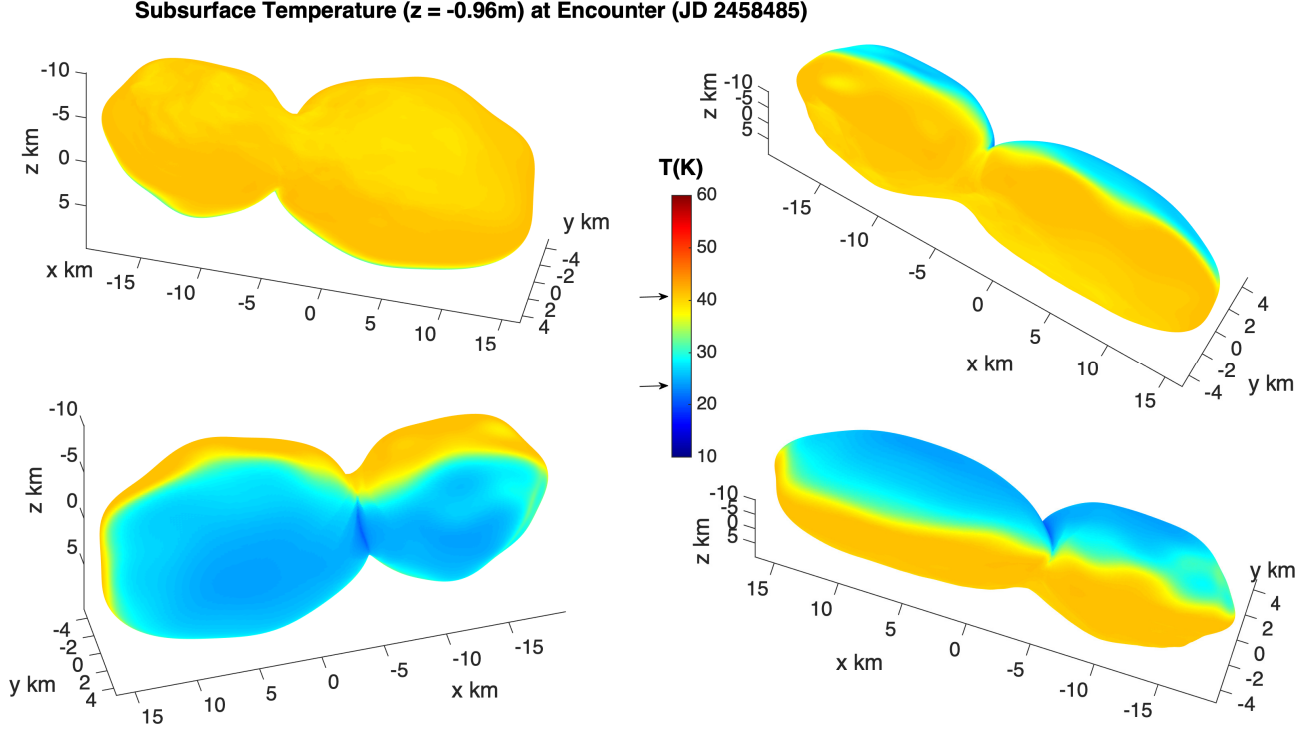


Figure 8. Four views of temperature at a depth of ~ 1 m at encounter day. The arrows on the colorbar show the range of temperature values at this depth. The four views are the same orientation as those shown in Fig. 6.

no ray-tracing calculation is needed. In other words no ray-tracing is needed if

$$\hat{\mathbf{n}}_i \cdot \hat{\mathbf{n}}_{\text{sun}} > \cos(\pi/2 - \beta_i) \geq 0. \quad (19)$$

This criterion considerably speeds up calculations. Formally then we define $f_{\odot,i}$ to be the daily average of $f_{\oplus,i}$, which involves an integral over one Arrokoth 15.9 hour day. We sample this integral using N_k equally spaced longitude values φ_k ranging from 0 to 2π . In other words we say

$$f_{\odot,i}(\lambda) \equiv \frac{1}{\hat{t}_{\text{day}}} \int_0^{\hat{t}_{\text{day}}} f_{\oplus,i}(\varphi(\hat{t}), \lambda) d\hat{t} \quad (20)$$

$$\approx \frac{1}{N_k} \sum_{k=1}^{N_k} f_{\oplus,i}(\varphi_k, \lambda). \quad (21)$$

In all of our calculations we choose $N_k = 16$.

3.4. Thermal Solution

We approach the solution to Eq. (13) on the assumption that the thermal response is purely periodic, which means to say that all transients have died away, therefore making this a so-called time asymptotic solution like used by Titus & Cushing (2012); Schloerb et al. (2015) and White et al. (2016). We opt for adopting this

assumption and the following Fourier transform based solution method owing to the spectral accuracy in produces, especially with respect to the importance of preserving the total conducted energy into and out of the interior over the course of one orbital period. As such, the solutions are represented as a truncated Fourier series in powers of the orbital frequency ω ,

$$\Theta_i = \sum_{n=0}^N \Theta_{i,n} e^{k_n z} e^{-i\omega n t} + \text{c.c.}, \quad (22)$$

in which

$$k_n = \left(\frac{i\rho C_p \omega n}{K} \right)^{1/2}, \quad \text{Re}(k_n) > 0, \quad (23)$$

where N is an integer that is about the sampling rate of the received flux $f_{\odot,i}$ (see further below). For each value of n , the functional forms in Eq. (22) are the exact solutions of the Fourier Transform of Eq. (13) where the amplitudes $\Theta_{i,n}$ are unknown and must be determined from enforcing boundary conditions. Eq. (22) automatically solves the lower thermal boundary condition Eq. (14). We observe that $\Theta_{i,0}$ is half of the deep interior temperature ($\equiv T_{\text{int},i}$), and so long as the thermal forcing is not aperiodic we note that $\equiv T_{\text{int},i}$ is time independent for a given facet, but may vary from facet to facet. The

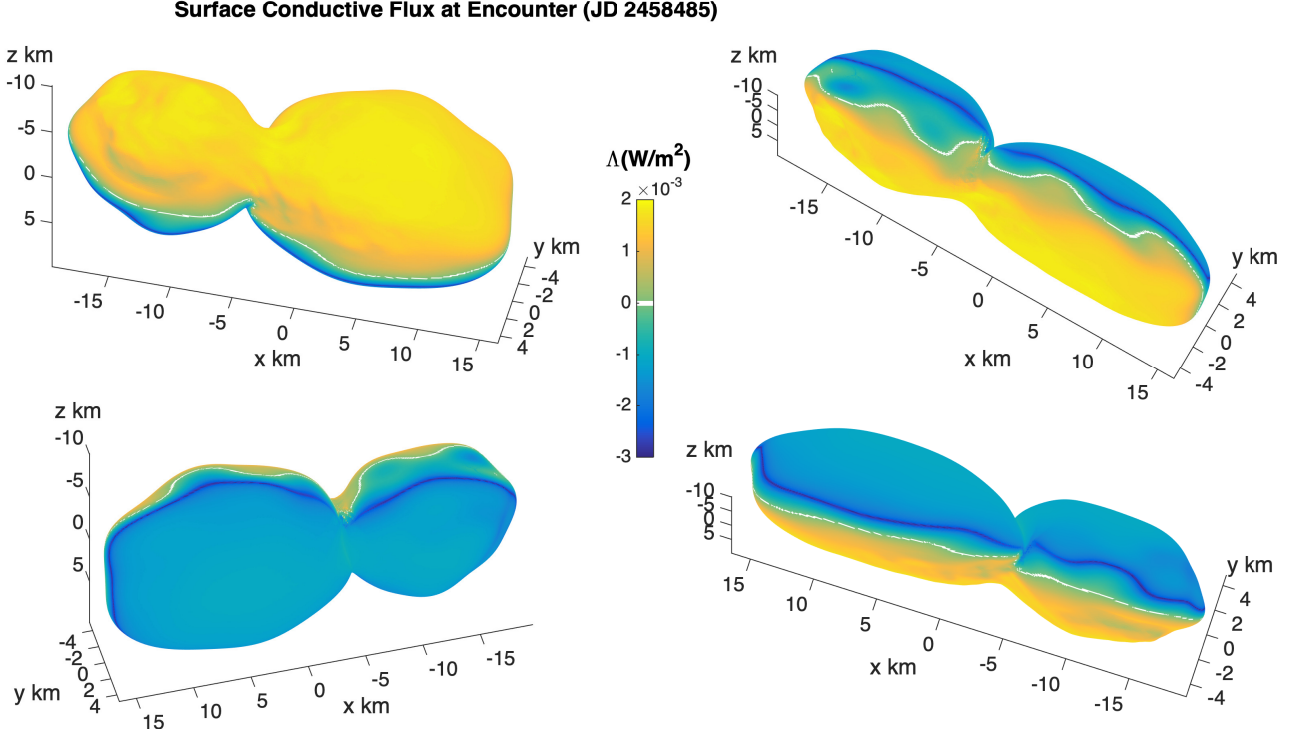


Figure 9. Four views of conductive flux ($\Lambda \equiv K\partial_z T_i$) at encounter day. The arrows on the colorbar show the range of flux values (also see Fig. 7). The white line shows the transition from inward and outward conductive flux. The four views are the same orientation as those shown in Fig. 6. The intense surface directed ring follows the temperature terminator (cf., Fig. 6).

advantage of this approach is that we do not have to directly calculate subsurface temperatures numerically as this information is encoded in the vertical structure function $e^{k_n z}$ for each Fourier mode n . For the sake of academic completeness we describe the rudiments of the solution approach in Appendix B, and discuss further in the Appendix C how this approach may be generalizable to configurations in which the conductivity changes value with depth, as might be the case if one is confronted with a physical situation in which very low thermal inertia refractories sit atop an otherwise highly conductive solid ice layer below (see also section 5). This multi-layer model was in fact used in generating the Arrokoth thermal solutions based on the 1962 facet model found on the Small Bodies Node PDS data repository (https://pds-smallbodies.astro.umd.edu/data_sb/missions/newhorizons/index.shtml), and is the reason we have included detailing this kind of layered solution approach in Appendix C.

With Eq. (22) in hand, it is straightforward to assess the surface thermal flux (Λ_i)

$$\Lambda_i \equiv K\partial_z T_i = K \sum_{n=1}^N k_n \Theta_{i,n} e^{-i\omega n t} + \text{c.c.} \quad (24)$$

The final stage involves determining the coefficients $\Theta_{i,n}$, which, once inverse Fourier transformed, gives the time series of T_i over the course of one cycle ω . The coefficients are determined using an iterative procedure sketched in the following: for notational ease we identify $f_i \equiv \epsilon_{\text{ir}} \sigma T_i^4$, then the boundary condition is

$$f_i = (1 - A)f_{\odot,i} + K\partial_z T_i + K_{ij}f_j. \quad (25)$$

The zeroth order solution is the solution to the above with the conductive term set to zero. Thus

$$f_i^{(0)} = \left(\mathbf{I}_{ij} - K_{ij} \right)^{-1} (1 - A)f_{\odot,i}, \quad (26)$$

which involves a matrix inversion – with \mathbf{I}_{ij} the identity matrix – followed by determining the first iterate temperature solution $T_i^{(1)}$ to

$$f_i^{(1)} = \epsilon_{\text{ir}} \sigma \left(T_i^{(1)} \right)^4 = f_i^{(0)} + K\partial_z T_i^{(1)}. \quad (27)$$

In this equation $f_i^{(0)}$ is known at all points along the orbit, thus it becomes a matter of solving for $T_i^{(1)}$. This is achieved by performing a fast Fourier Transform of Eq. (27) into frequency domain followed by using a Newton-Raphson routine⁴ to solve for the Fourier components

⁴ For example, https://en.wikipedia.org/wiki/Newton's_method.

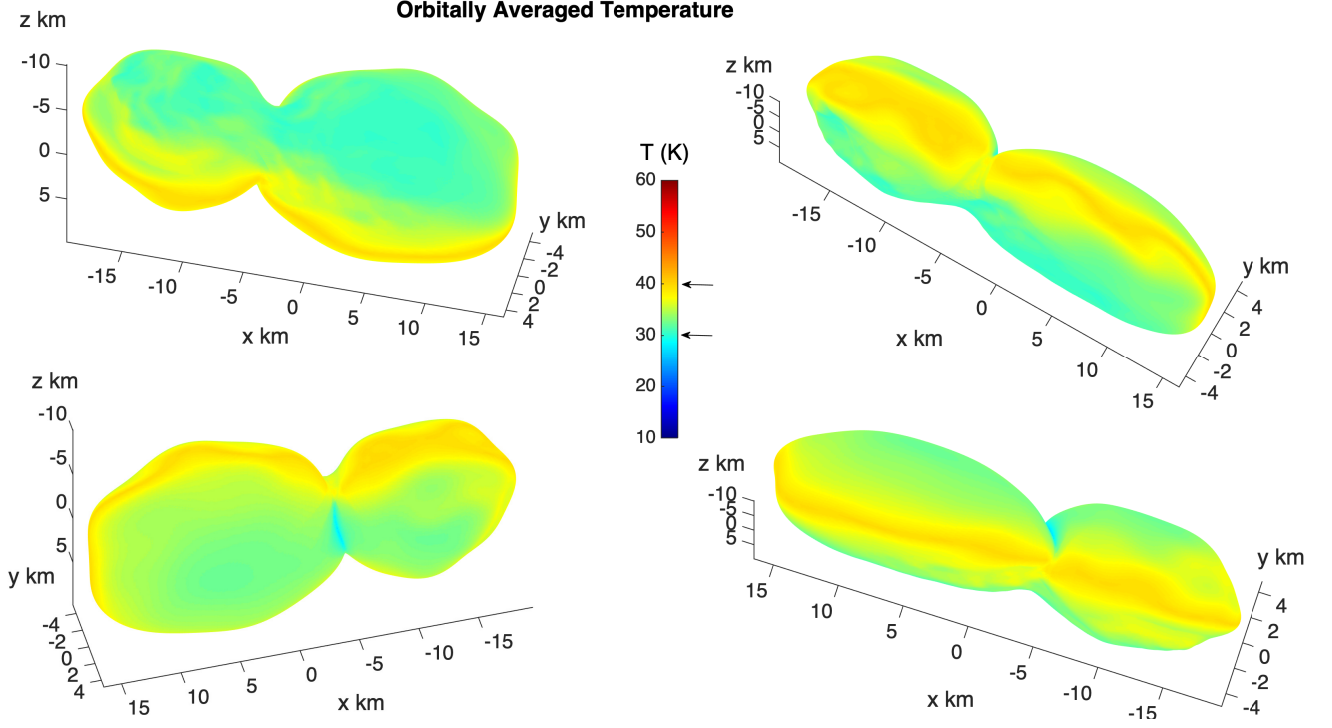


Figure 10. Four views of orbitally averaged surface temperature. The four views are the same orientation as those shown in Fig. 6. The range of temperatures are shown with arrows, see also Fig. 12.

$\Theta_{i,n}^{(1)}$. The received flux, as well as the solution of the surface temperature field, is well represented with a $N = 30$ Fourier mode decomposition. We have assessed the robustness of these $N = 30$ results against solutions generated up to $N = 300$ finding characteristic differences in the temperature field (for any given facet) differing by less than 1 part in 10^5 . For a given face, we demand for convergence that successive changes in each $\Theta_{i,n}^{(1)}$ be less than 10^{-4} , which is usually achieved in 6 or less sub-iterations. All higher iterations $m \geq 2$ involve calculating

$$\epsilon_{\text{ir}} \sigma \left(T_i^{(m)} \right)^4 = K \partial_z T_i^{(m)} + (1 - A) f_{\odot,i} + K_{ij} f_j^{(m-1)} \quad (28)$$

$$f_i^{(m)} = \epsilon_{\text{ir}} \sigma \left(T_i^{(m)} \right)^4, \quad (29)$$

where, as before, the first of the above equations is solved in Fourier frequency space, while the second takes that solution and expresses it in the time domain, calculating the matrix product $K_{ij} f_j^{(m)}$ in the time domain, and then feeding the result forward to the next iteration, $m \rightarrow m + 1$. Note that while this procedure involves one large matrix multiplication per iteration, it is not the main bottle-neck in the calculation, but rather the Newton-Raphson stage, for which values of $m \geq 2$ tends to converge in 1-2 sub-iterations owing to the closeness of the initial guess to a converged solution. For this

particular system, in which the characteristic Spencer number Γ is low, we find that satisfactory convergence is achieved in one ($m = 1$) iteration.

This calculation is run in parallel using four 3.1 GHz Intel Cores (i7). The temperature solution for each facet (including all sub-iterations) takes less than 0.004 cpu seconds/processor for $N = 30$ and 0.09 seconds/processor for $N = 300$. We find that it takes approximately 40 minutes to generate a full solution with one iteration for the 10^5 facet model when $N = 300$, whereas it takes a little over 3 minutes when $N = 30$. All results displayed in this study are done with $N = 300$.

We close this section by defining the orbitally averaged *flux temperature* $T_{a,i}$, which is, for each facet, the orbital average of the solution to Eq. (15) in the infinitely insulating limit (i.e., $K \rightarrow 0$). Given the preceding discussion, this amounts to the solution to

$$\epsilon_{\text{ir}} \sigma T_{a,i}^4 = \frac{1}{P} \int_0^P f_i^{(0)}(\lambda(t)) dt, \quad (30)$$

in which P is Arrokoth's orbital period, and where $f_i^{(0)}$ – given in Eq. (26) – is understood to be a time-dependent function of the subsolar latitude $\lambda(t)$. This quantity is a proxy for the total received insolation for each facet. Given Arrokoth's high obliquity, we expect $T_{a,i}$ to be relatively higher in the regions experiencing

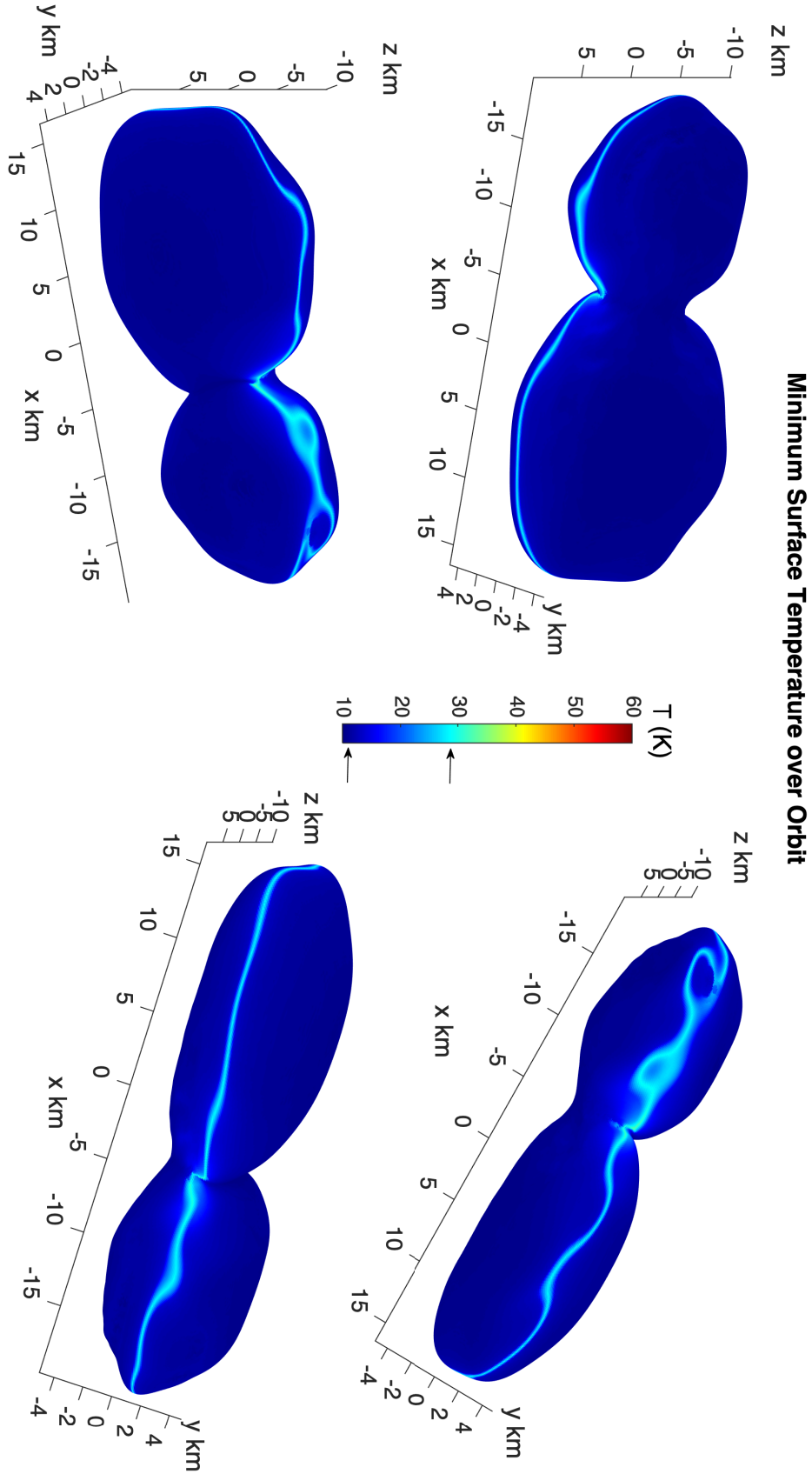


Figure 11. Four views of absolute minimum surface temperature of each facet over the course of one orbit. The four views are the same orientation as those shown in Fig. 6. The range of temperatures are shown with arrows, see also Fig. 12. Note the higher temperatures running within the equatorial zone and occasionally outlining the putative rims of cratered morphology lying in the tropical zone.

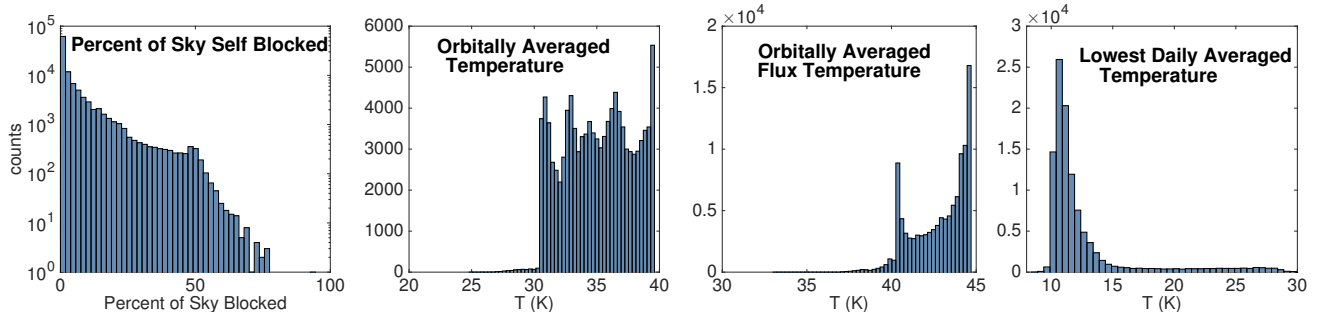


Figure 12. Histogram plots for various orbital scale quantities. Model assumes $\mathcal{I} = 2.54$ tiu, $A = 0.06$, and $\varepsilon = 0.9$. Vertical axis corresponds to number of facets. The panels are: (left panel) percent of body self-obscuration in reference to Fig. 3, (middle left) orbitally averaged surface temperature $T_{\text{int},i}$, (middle right) orbitally averaged flux temperature $T_{\text{a},i}$, (right) minimum surface temperature over the course of one orbit.

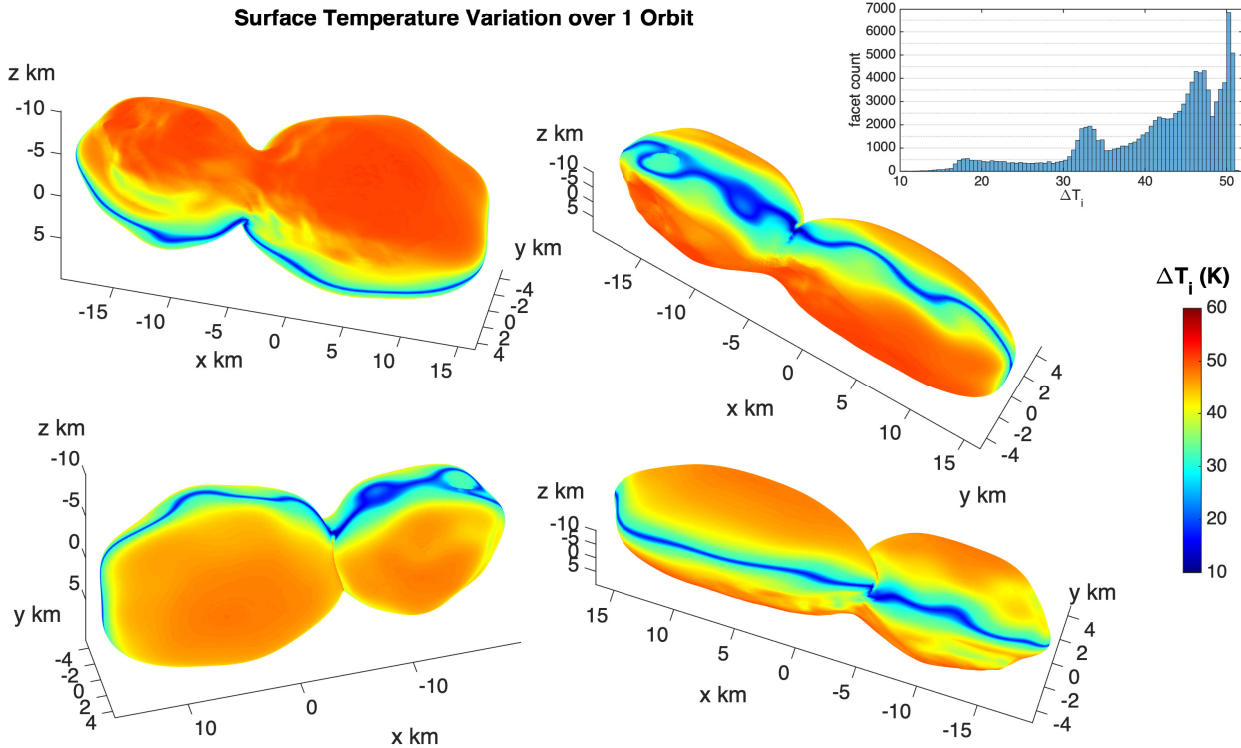


Figure 13. Four views of full temperature variation over the course of one orbit ΔT_i . The four views are the same orientation as those shown in Fig. 6. Far upper right graph shows a histogram of ΔT_i .

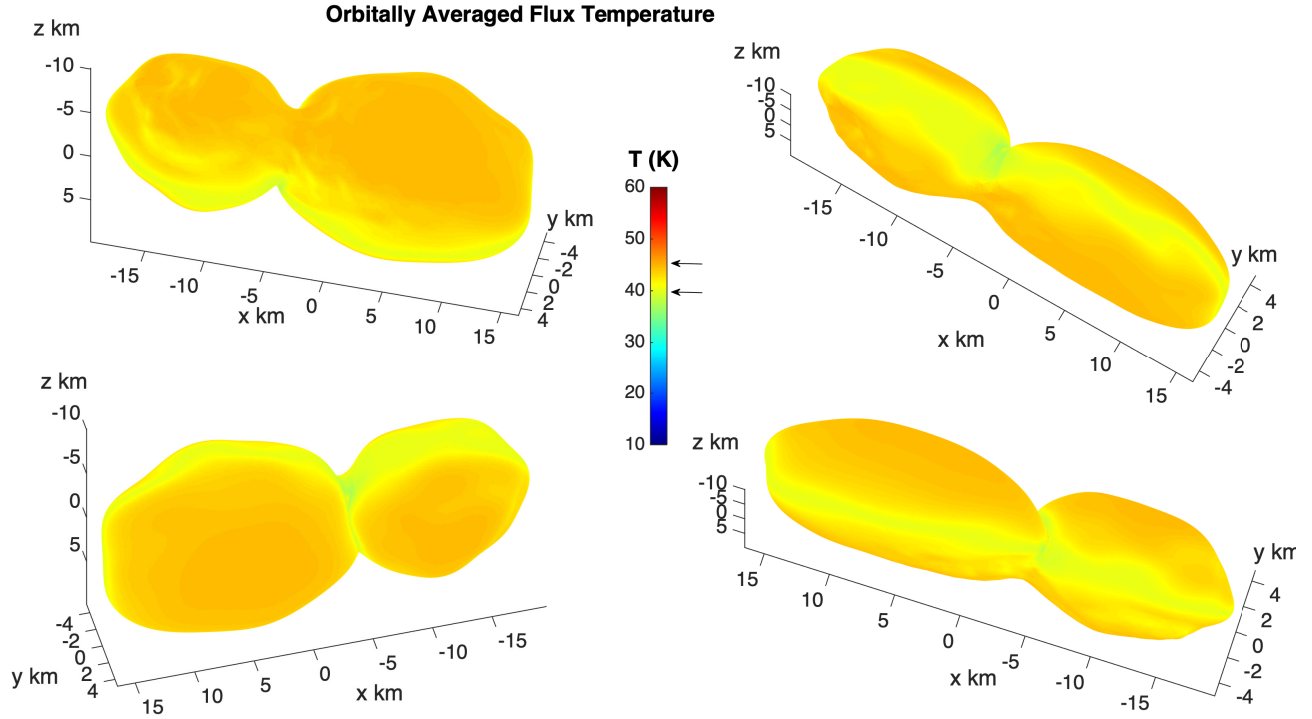


Figure 14. Four views of orbitally averaged flux temperature $T_{a,i}$. The four views are the same orientation as those shown in Fig. 6. The range of temperatures are shown with arrows, see also Fig. 12.

extreme polar winters and summers ($|\lambda| \gtrsim 10^\circ$) compared to Arrokoth’s perpetually diurnal equatorial zones ($|\lambda| \lesssim 10^\circ$). Henceforth, we designate as *polar region* or *polar zone* latitudes that satisfy $|\lambda| \gtrsim 10^\circ$, while ascribing *tropical zone* or *equatorial zone* to latitudes satisfying $|\lambda| \lesssim 10^\circ$ (e.g., as in the usage of Earle et al. 2017).

4. FULL BODY THERMAL MODEL: RESULTS

4.1. Encounter Day Views

In Fig. 6 we present an example temperature map of Arrokoth viewed on encounter day (January 1, 2019 or Julian Date 2458485) on the assumption that $\mathcal{I} \approx 2.5$ tiu, which, in turn, corresponds to an effective Spencer Number $\Gamma_{\text{eff}} \approx 0.0082$ (with $\bar{T}_s \approx 59\text{K}$), where we follow the definition found in Eqs. (9-10) and adopting $\bar{f}_\odot = f_\odot(r = 44\text{AU})$. On this day, the subsolar latitude (λ_{ss}) was $\lambda_{ss} \approx -61.86^\circ$ and Arrokoth was ≈ 43.24 AU from the sun (see also Fig. 5). Four views are shown in Fig. 6: The upper left panel shows the approach view, where the simulated body specific subspacecraft coordinates are at $\varphi = -46.9^\circ$, $\lambda = 76^\circ$, while the lower left panel shows the departure view with nominal subspacecraft coordinates $\varphi = 46.9^\circ$, $\lambda = 284^\circ$. The latter view position closely approximates the view from the spacecraft when the REX (CA08) scan was made.

For these parameters the predicted surface temperatures ranges from 10 K to 60 K. The distribution of temperatures, in terms of facet counts, is shown in the first panel of Fig. 7. A cursory view of the upper left panel of Fig. 6 displays the propensity for high temperatures (in the vicinity of 57-60K) over most of the flattened and exposed real estate of the encounter hemisphere ranging from the south pole down to $\lambda = -10^\circ$ or so. The view from the REX observation point (lower left panel of Fig. 6) shows the surface temperature is dominated by the winter side values (around 12-13 K) with a sliver of high temperatures along the top outer rim. The temperature transitions from the winter side lows to the summer side highs through the equatorial region, with the transition occurring across a narrow band of tropical estate.

Fig. 8 shows a predicted temperature map at approximately 1m below Arrokoth’s surface. The input parameters are as those shown in Fig. 6. The temperatures at this depth range from about 40K down to 25K. Notably, the temperatures at this depth are slightly cooler at high summer side latitudes than they are at latitudes approaching the equator (the differences being 3-4 K). This is to be expected since tropical zone latitudes never go into polar night over the course of one orbit, which means that the temperature there never get nearly as cold as they do in the poles (see further below). The

winter side temperatures, on the other hand, do not show this slight inversion. The reason for this is likely due to the winter-side part of the shape model not being nearly as flattened as the imaged encounter hemisphere – but we caution against drawing strong conclusions here owing to the true uncertainty of the topography of the unseen hemisphere.

Fig.9 shows the instantaneous daily averaged conductive flux at the surface at the day of the encounter. Once again the view and input parameters are the same as those shown for the two prior figures. The figure confirms one’s intuition, in which the thermal flux is interior directed on the lit summer side of Arrokoth ($\sim 0.002 \text{ W/m}^2$, i.e.,), while the conductive flux is surface directed on Arrokoth’s winter side ($\sim -0.0015 \text{ W/m}^2$). We have delineated where the transition occurs from outward to inward flux as well. One notable feature is the appearance of a relatively high intensity ring of surface directed thermal flux ($\sim -0.003 \text{ W/m}^2$) along the temperature terminator. This ring coincides with the location of the pre-sunrise edge of Arrokoth’s surface, where the temperature gradient along the surface is greatest (e.g., compare against the surface temperatures shown in Fig. 6). We find this ring to closely follow the illumination terminator over the course of Arrokoth’s solar revolution.

Fig. 7 shows several facet count histograms for various quantities at encounter day. These include a distribution of surface temperatures to be compared with Fig. 6 and surface fluxes of Fig. 9. The intense ring of surface fluxes appears as a long tail below the distribution mode at $\Lambda \approx -0.0015 \text{ W/m}^2$. We have also shown the distribution of instantaneous total received illumination flux at every facet, which includes both direct received sunlight as well as illumination received from reradiation from other “seen” facets. The distribution shows a strong mode at around 0.6 W/m^2 , while including a large number of facets receiving nearly zero flux (i.e., only CMB). We have separated out from the total received flux only the flux received from surface reradiation (labelled as flux received from surrounding landscape). The irradiation received in the form of surface re-radiation ($\sim 0.02 \text{ W/m}^2$) amounts to less than 5% of the total irradiation. Once again this appears to be due to Arrokoth’s relatively muted local relief despite its otherwise flattened global shape. These trends are consistent with those based on low-order 1962 facet model reported in Grundy et al. (2020).

As a final reflection, the behavior here ought to be compared to temperature predictions done for a body with a neck but much more marked topography (e.g., 67P/Churyumov-Gerasimenko), would be interesting in

its own right, in terms of the role of re-radiation, shadowing, etc. (Hu et al. 2017).

4.2. Orbital Timescale Features

Adopting $\mathcal{I} = 2.54$ tiu, as in the prior section, we display various orbital timescale properties. In Fig. 10 we showcase the orbitally averaged surface temperature of each facet. This quantity also corresponds to the asymptotic interior temperature (i.e., $T_{\text{int},i}$) descriptive of subsurface positions exceeding several thermal skin depths. For all regions of the body except for a narrow equatorial band ($\sim \pm 10^\circ$), the deep interior temperature is in the low 30K-35K range. On the other hand, $T_{\text{int},i}$ in the equatorial band is closer to 40K. These trends make sense given that polar winters last long enough for all the received and thermalized summer time solar energy to radiate away. Since the equatorial “tropical” zone always sustains a diurnal insolation pattern, the received solar insolation over those regions never sufficiently radiates away to lower the surface temperatures nearly as much before the Sun rises again. This effect is most dramatically illustrated in Fig.11 showing the absolute minimum temperature any one facet experiences over the course of one orbit. Almost the entirety of Arrokoth’s surface, including substantial parts of the tropical zone, experiences minimum temperatures in the range of 10K-15K. But, a very thin sliver of real estate following the equator and occasionally outlining cratered morphology regions found within the tropical zone, show minimum temperatures as high as 30K. The distribution of these temperatures are shown in Fig. 12.

The interior depths of the equatorial zone are thus warmer than the polar region despite the fact that these parts receive overall less insolation over the course of one orbit. This is clear when viewing the predicted flux temperature as defined in Eq. (30). $T_{a,i}$ is a proxy for the total irradiation received on any given facet and is shown in Fig. 14. As an orbital average, the tropical zones receive far less solar insolation, with $T_{a,i} \sim 40\text{K}$, than the polar regions, where $T_{a,i} \sim 45\text{K}$ (see also third panel of Fig. 12). Yet despite this, the averaged surface temperature in the tropics is much higher than the poles.

5. CONNECTING TO REX OBSERVED BRIGHTNESS TEMPERATURES

The REX radio flux density measurements made during the CA08 observing sequence, together with the shape model for Arrokoth, leads to an Arrokoth-disk averaged x-band brightness temperature $T_{b,\text{obs}} = 29 \pm 5\text{K}$ (Grundy et al. 2020). This result has been reaffirmed in a more comprehensive analysis (Bird et al. 2022). The brightness temperature depends on various properties of

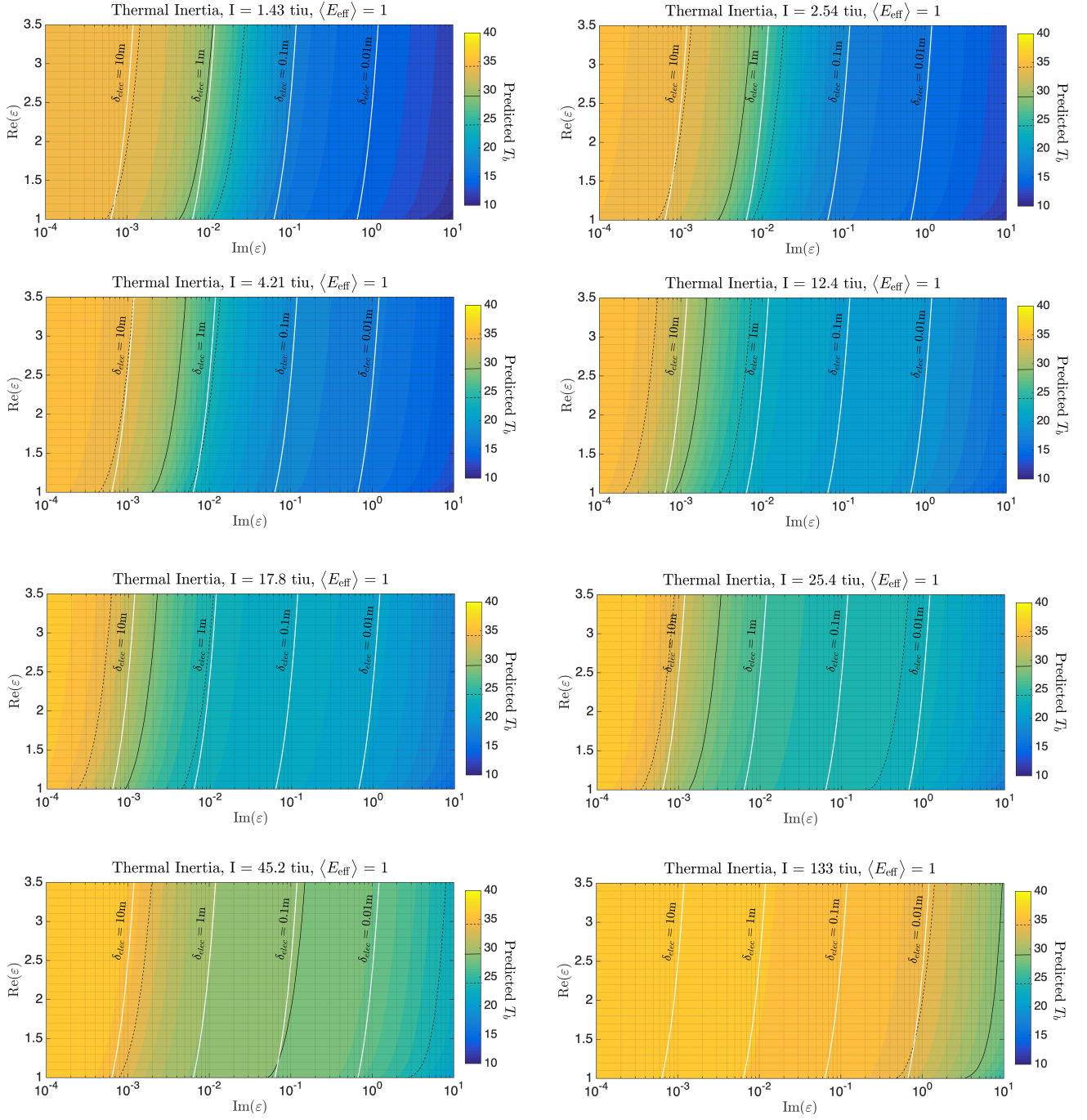


Figure 15. Predicted brightness temperatures based on subsurface radiative transfer analysis for $\langle E_{\text{eff}} \rangle = 1$. Several values of \mathcal{I} shown. White contours denote several values of electric skin depth. Note the weak dependence on the ϵ' (denoted on graphs as $\text{Re}(\epsilon)$).

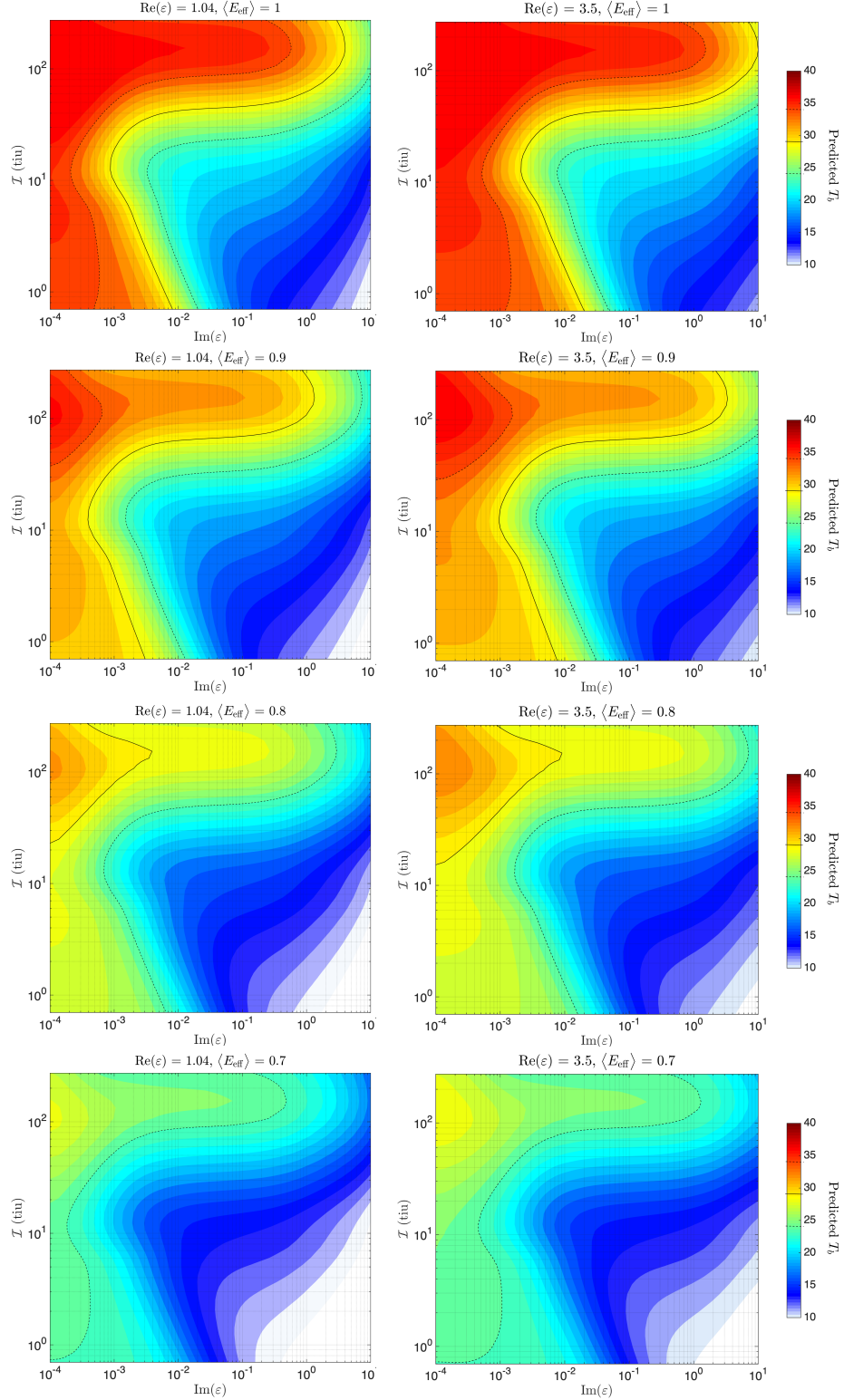


Figure 16. Predicted brightness temperatures T_b for the CA08 observation. For input values of $\varepsilon' \equiv \text{Re}(\varepsilon)$ and $\langle E_{\text{eff}} \rangle$ predicted T_b shown as a function of $\varepsilon'' \equiv \text{Im}(\varepsilon)$ and \mathcal{I} : (left column) $\varepsilon' = 1.04$, (right column) $\varepsilon' = 3.50$. Successive rows corresponding to decreasing values of $\langle E_{\text{eff}} \rangle$. Black contours denote $T_b = 29\text{K}$ while dotted black contours represent $T_b = 24\text{K}$ and 34K levels. The right column might be considered representative of pure methanol ice of zero porosity, while the left column could be the same with porosity of 60%.

Arrokoth’s near surface materials. In order to calculate a model prediction for the brightness temperature that we here simply call T_b , it is necessary to perform a radiation transfer analysis that relates Arrokoth’s interior kinetic temperature $T(z)$ – as detailed in previous sections – and its X-band thermal and refractive properties to $T_{b,obs}$. In other words,

$$T_{b,obs} = T_b(\mathcal{I}, \varepsilon', \varepsilon'', \langle E_{\text{eff}} \rangle), \quad (31)$$

in which T_b depends on knowledge of the material’s thermal inertia, the value of the real and imaginary part of its X-band dielectric constant/permittivity $\varepsilon = \varepsilon' + i\varepsilon''$ ⁵, and its effective X-band emissivity $\langle E_{\text{eff}} \rangle$. These 4 a priori unknown parameters may themselves have some kind of depth-dependence, but for our purposes here we take them to be constants. In principle, there exists a relationship between \mathcal{I} , ε' , ε'' , and $\langle E_{\text{eff}} \rangle$ that produces values of T_b equal to $T_{b,obs}$. Anticipating our discussion in section 6.1, at best we will be able to only circumscribe this relationship between the four unknown parameters.

Utilizing the approach detailed in Section 3, we develop a suite of near surface thermal solutions for several values of the thermal inertia, i.e., in the range $0.5 \text{ tiu} < \mathcal{I} < 275 \text{ tiu}$ on 35 equally spaced values along a logarithmic scale. Together with our adopted values of ρ and C_p , this range of \mathcal{I} values corresponds to a characteristic orbital timescale skin depth values,

$$\ell_{\text{orb}} \equiv \mathcal{I} / \rho C_p \sqrt{\omega}, \quad (32)$$

that fall into the range $22 \text{ cm} \lesssim \ell_{\text{orb}} \lesssim 120 \text{ m}$, where ℓ_{orb} ’s definition is based on the setting $n = 1$ into the absolute value of the inverse of the thermal wavenumber defined Eq. (23). It is sufficient to use $N = 30$ Fourier modes to generate this solution array (see section 3.4). We develop solutions in which for depths below 10 meters from the surface the thermal conductivity transitions to a fixed constant value for porous H₂O ice (e.g., $K = 1 \text{ W/m/K}$, Klinger 1980, corresponding to a value $\mathcal{I} = 295 \text{ tiu}$ – also see sec. 3.4 and Appendix C).

With these temperature solutions in hand, we then employ the radiative transfer solution method outlined in de Kleer et al. (2021) to produce a set of predicted \tilde{I}_ν that finally relate to T_b via Eq. (31). For the transfer solutions we consider the following ranges of the remaining parameters: $1 \leq \varepsilon' \leq 3.5$ at 70 equally spaced values on a linear scale, $10^{-4} \leq \varepsilon'' \leq 10$ at 75 equally

spaced values on a logarithmic scale, and four values for, $\langle E_{\text{eff}} \rangle = 0.7, 0.8, 0.9, 1.0$. These parameter choices follow those also considered in Bird et al. (2022). Further details of the solution method as implemented are found in Appendix D. We note that the electrical skin depth, δ_{elec} , approximately relates to ε via

$$\delta_{\text{elec}} = \frac{\lambda}{2\pi} \frac{\sqrt{\varepsilon'}}{\varepsilon''}, \quad (33)$$

in the $\varepsilon'' \ll 1$ limit of its formal definition found in Eq. (D24). Finally, we do not account for Fresnel reflection at the interface.

In our companion study, Bird et al. (2022, this issue) also develop $T_{b,obs}$ predictions based on the thermal solutions. The differences lie in the approaches taken to solve the radiative transfer problem: As each spacecraft visible facet i has its own unique vertical temperature profile $T_i(z)$, this work develops a facet-by-facet solution to the transfer problem followed by taking a facet area weighted average across the visible disk of Arrokoth to derive $T_{b,obs}$. On the other hand, Bird et al. (2022) develop a simpler estimate for $T_{b,obs}$ based on a single effective vertical temperature profile $\bar{T}(z)$, which is constructed as a facet-area weighted average of all $T_i(z)$, and a surface averaged facet norm with associated cosine of the spacecraft inclination angle $\cos \theta_t$. Formally speaking the two approaches are not necessarily commensurate – as the average of products is not necessarily equal to the product of averages (also see discussion in Appendix D – but in this case here we find that the results happen to be in mutual agreement.

We observe several trends. Most prominent is that for given values of \mathcal{I} there is only a weak dependence of on ε'' as ε' varies from 1 to 3.5 (see Fig. 15). Fig. 16 displays contour levels of several predicted T_b as a function of ε'' and \mathcal{I} for several fixed values of ε' and $\langle E_{\text{eff}} \rangle$. Except for $\langle E_{\text{eff}} \rangle = 0.7$, the $T_b = 29\text{K}$ contour exists for all input parameter values considered. In section 6.1 we further discuss and interpret the implications of these solutions, especially with respect to known candidate materials. However we can make one clear observation here that solutions in which $\langle E_{\text{eff}} \rangle = 0.7$ appear to be ruled out as the $T_b = 29\text{K}$ contour fails to even register under these circumstances and, at best, only the low end of the REX observation is predicted ($\sim 24\text{K}$) but does so at very low (nearly transparent) values of $\varepsilon'' (< 10^{-3})$ for $\mathcal{I} \lesssim 40\text{tiu}$, while the predicted $T_b = 24\text{K}$ contour is plausible only for $\mathcal{I} > 100\text{tiu}$ at considerably larger upper bound values for ε'' , i.e., in the range of 0.1 and 1.

We pose another question: Given $\varepsilon', \mathcal{I}$ and $\langle E_{\text{eff}} \rangle$, what value of ε'' yields a predicted T_b during the CA08

⁵ Note, hereafter all values of ε are scaled in units of vacuum permittivity $\varepsilon_0 \approx 8.85 \times 10^{-12} \text{ F/m}$, where F is in units of Farads.

observation? We define this critical value as ε_c'' and we derive these values using interpolation methods based on the solutions determined above. Fig. 17 displays $\log \varepsilon_c''$ as a contour plot for $\langle E_{\text{eff}} \rangle = 0.9, 1.0$. We have left out doing this exercise for the $\langle E_{\text{eff}} \rangle = 0.7$ and 0.8 cases because $T_b = 29\text{K}$ registers as a possibility only for a limited range of \mathcal{I} values for the latter case and none at all for the former case (see Fig. 16). It is notable that in both cases $\varepsilon_c'' < 0.05$ for values of $\mathcal{I} < 70$ tiu. This analysis also predicts that the material is very nearly transparent in the X-band (i.e., $\varepsilon_c'' \approx 0.001$ or less) for values of $2 \text{ tiu} \lesssim \mathcal{I} \lesssim 40 \text{ tiu}$. We revisit this in the next section.

A question that will be addressed later is if $T_{b,\text{obs}}$ might be explained by X-band radiation emanating from well below the orbital time scale skin-depth. To help answer this question, we define T_{deep} to be the visible-facet weighted observed X-band brightness temperature at $\langle E_{\text{eff}} \rangle = 1$ for values of the dielectric skin depth – δ_{elec} defined in Eq. (D24) – greatly exceeding ℓ_{orb} . In other words, it corresponds to a visible-facet weighted disk averaged *deep subsurface temperature* sampled by *nearly* transparent X-band radiation sampling the deep interior.⁶ From this interpretation it follows that

$$T_b(\langle E_{\text{eff}} \rangle, \delta_{\text{elec}} \gg \ell_{\text{orb}}) \rightarrow \langle E_{\text{eff}} \rangle \cdot T_{\text{deep}}. \quad (34)$$

In Fig. 18 we plot T_{deep} as a function of \mathcal{I} . Inspection of the figure clearly shows that values of $\langle E_{\text{eff}} \rangle = 0.7$ are clearly precluded from predicting even $T_b = 24\text{K}$ on the low \mathcal{I} end, while possibly permitting $T_b = 29\text{K}$ on the high \mathcal{I} end (i.e., > 150 tiu). We return to discussing this in the next section.

6. DISCUSSION

6.1. On the thermophysical properties of Arrokoth's subsurface materials

There are no independent measures of the four input parameters that go into these thermal solutions constructed here. Unfortunately, there is very little one can conclude with certainty about their values or properties based on the New Horizons' single REX scan (see also Bird et al. 2022). Partly given its laboratory data availability and partly given that planetesimals are thought to be substantially composed of H_2O ice, we mainly focus on the property of water ices despite there being no direct evidence for it on the surface. This H_2O ice which

may also have a tholin covering. We save for future analysis the possibility for other less-well laboratory studied materials to explain the REX observation.

The primary concern here is that there is a relationship between ε' , ε'' , \mathcal{I} , and $\langle E_{\text{eff}} \rangle$ that yield a predicted $T_b = 29\text{K}$ corresponding to the brightness temperature measured during the CA08 REX observation. One example relationship is the quantity $\varepsilon'' = \varepsilon_c''(\varepsilon', \mathcal{I}, \langle E_{\text{eff}} \rangle)$ developed in the previous section and, for example, displayed in Fig. (17). Aside from Arrokoth harboring surface methanol, there is no other information about the body's surface or subsurface composition. As such, we are here relegated to speculating about the possible values of these quantities in relation to other known bodies of the outer solar system. In this section we consider various facets of the problem and we conclude by offering what we consider to be our favored interpretation.

6.1.1. Permittivity/Dielectric Constant

Perhaps most confounding for this analysis are the uncertain values of ε' and ε'' , the latter of which strongly controls the material's attenuation of the X-band signal through the subsurface medium especially when $\varepsilon'' \ll 1$, e.g., see Eq. (D24). We consider several possibilities in order of increasing speculation:

- Methanol, likely a significant constituent of Arrokoth's near surface, has a value of $\varepsilon' \approx 3.52 \pm 0.05$, but with no corresponding measurement of ε'' (Le Gall et al. 2016). This same study also reported a value of $\varepsilon' \approx 3.42 \pm 0.05$ for the similar hydrocarbon ethanol. One can estimate an effective ε' on the assumption a certain ice fraction of vacuum porosity (p hereafter) following the Maxwell Garnet empirical formula for vacuum mixtures discussed in Bird et al. (2022). If, for example, the upper layer is composed of pure methanol with $p = 0.6$, then it would have an effective $\varepsilon' \approx 1.04$ corresponding to the left column of solutions shown in Fig. 16, while the $p = 0$ solution would be the same figure's right column.
- Based on laboratory work of Paillou et al. (2008), which examined the dielectric properties of various tholin-like materials, Bird et al. (2022) compiled a range of possible effective ε values of several types of porous tholins based on the same prescription for mixtures. For porosity p in the 0.60 to 0.80 range: powdered tholins exhibits values of ε' from 1.05 to 1.01, with ε'' values ranging from 1×10^{-3} to 5×10^{-4} ; while for two types of compact tholins examined ε' correspondingly ranges from 1.5 to

⁶ We are careful to note that there is a limit here as well. One might imagine the X-band radiation is so transparent through Arrokoth's interior that it could also sample its sunlight side. However this would suggest unrealistically low values of $\varepsilon'' \ll 10^{-6}$.

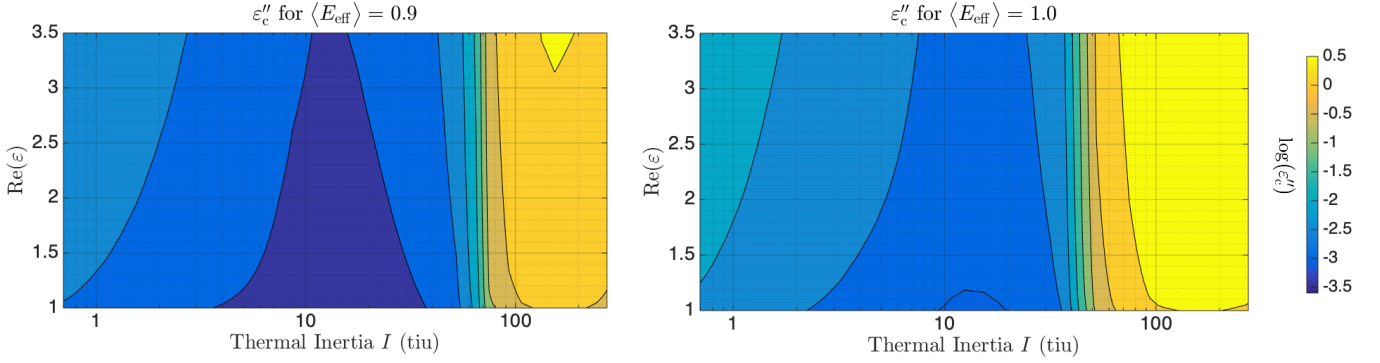


Figure 17. Value of ε_c'' that yields $T_b = 29\text{K}$ during CA08 for $\langle E_{\text{eff}} \rangle = 0.9, 1.0$. For these values of $\langle E_{\text{eff}} \rangle$ this analysis predicts that the material is very nearly transparent in the X-band ($\varepsilon_c'' \lesssim 0.002$) for $1 \text{ tiu} < \mathcal{I} < 40 \text{ tiu}$.

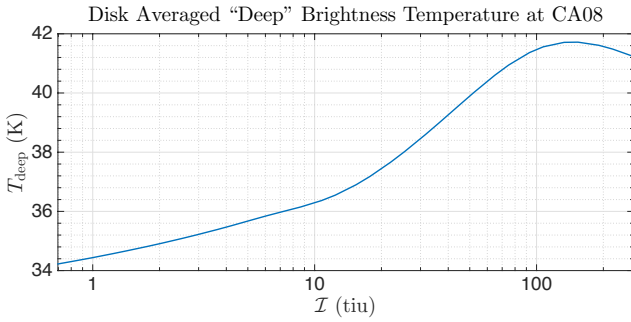


Figure 18. The disk averaged “deep” temperature T_{deep} as a function of \mathcal{I} , predicted for CA08.

1.2 together with ε'' falling somewhere between 4.2×10^{-3} and 1.5×10^{-3} .

- Arrokoth’s subsurface materials might resemble the “dirty” ice thought to comprise the nucleus of comets like 67P. Heggy et al. (2012) have compiled several known measurements of $\varepsilon = \varepsilon_{\text{mix}}$ of matrix ice with variable dust-to- H_2O mixtures with mixture fraction $0 < \phi_{\text{mix}} < 1$. The measurements were made at wavelengths a factor 10-50 larger than the X-band. From these they compile an empirical relationship for $\varepsilon'_{\text{mix}}$ and $\varepsilon''_{\text{mix}}$ as a function of ϕ_{mix} , as well as a weak dependence on T . For $T = 30\text{K}$ and $p = 0.5$ application of their relationship predicts for $\phi_{\text{mix}} \ll 1$ that $\varepsilon'_{\text{mix}} \approx 1.42$ and $\varepsilon''_{\text{mix}} \approx 10^{-4}$, while for $\phi_{\text{mix}} \rightarrow 1$ $\varepsilon'_{\text{mix}} \approx 2.90$ and $\varepsilon''_{\text{mix}} \approx 4 \times 10^{-2}$. These values will be somewhat smaller in bulk for higher porosities at fixed ϕ_{mix} . Similarly, Brouet et al. (2015) compiled ε' values for an ice mixture comprised of H_2O and the lunar regolith simulant JSC-1A. For porosities $p \approx 0.6$ they find $1.5 < \varepsilon' < 2.25$, depending on mixture fraction (e.g., see Figure 10 of Brouet et al. 2015); however, no values for ε'' were reported.

6.1.2. X-band Emissivity

Bird et al. (2022) compile a known list of the radio emissivity of the Kronian moons at $\lambda = 2.2\text{cm}$ based on Cassini RADAR observations. The color and albedos of these objects vary widely, with corresponding emissivity range of roughly $0.6 < \langle E_{\text{eff}} \rangle < 1$. However, if one focuses on the darkest of these objects (i.e., those with the lowest albedos comparable to Arrokoth) we find, for example, Iapetus’ leading dark side has $\langle E_{\text{eff}} \rangle \approx 0.87$ (Le Gall et al. 2014) while for Phoebe $\langle E_{\text{eff}} \rangle = 0.92$ (Ostro et al. 2006). If these bodies’s surface materials are analogs to Arrokoth’s, then supposing $\langle E_{\text{eff}} \rangle = 0.9$ for it would not be unreasonable.

In reference to our preceding discussion, it seems $\langle E_{\text{eff}} \rangle = 0.7$ is highly unlikely. One might argue by inspecting the deep temperature solutions shown in Fig. 18 that $T_b = 29\text{K}$ is achievable for $\langle E_{\text{eff}} \rangle = 0.7$ on the high \mathcal{I} end (i.e., the product $\langle E_{\text{eff}} \rangle \cdot T_{\text{deep}}$ yielding 29 K), but cross-referencing that against the $\langle E_{\text{eff}} \rangle = 0.7$ row of Fig. 16 would imply that this is feasible only for very large electric skin-depths, corresponding to $\varepsilon'' \ll 10^{-4}$. Given the discussion in the previous section we know of no plausible materials that would exhibit such highly transparent qualities. Performing the same cross-comparison a similar line of reasoning applies for rejecting $\langle E_{\text{eff}} \rangle = 0.8$ solutions for values of $\mathcal{I} < 20 \text{ tiu}$. However we see from the penultimate row of Fig. 16 that $T_b = 29\text{K}$ is achievable for $\langle E_{\text{eff}} \rangle = 0.8$ as it corresponds to physically reasonable values of $10^{-4} < \varepsilon'' < 10^{-3}$ in the thermal inertia range $20 \text{ tiu} < \mathcal{I} \lesssim 300 \text{ tiu}$. Based on the discussion, of the following section we also lean toward treating this case as unlikely (but not ruled out) on account of identifying plausible materials with such high bulk thermal inertias at such low temperatures and porosities.

6.1.3. Thermal Inertia

TNOs and KBOs as analogs. The 1-10 tiu \mathcal{I} range of values reported in Lellouch et al. (2013) for KBOs corresponds to daytime measurements that probe their surface materials down to their diurnal skin depths, which are in the vicinity of a few mm. Such low thermal inertias, which ought roughly be considered body averages, can be interpreted as indicating the presence of a very porous matrix of weakly loaded grains whose grain-grain radii of contact (a) are much smaller than the grain size (radius R_g). Since the ratio $h \equiv a/R_g$ (sometimes known as the Hertz factor) controls grain-to-grain heat conduction, small values of h – perhaps due to weak loading – coupled to high porosity conditions leads to thwarted effective heat conduction (see further below, and also Howett et al. 2010; Ferrari & Lucas 2016; Ferrari 2018). Therefore, it might not be unreasonable to suppose such fluffy low thermal inertia material extends much deeper than a few mm on small-sized KBOs like Arrokoth as little material compaction is expected under such low gravities ($\sim 1\text{mm/s}^2$) over its natural history – unless its surface experienced sufficient impacting events, but this appears to be ruled out on the basis of the relatively few observed impact features (Stern et al. 2019; Spencer et al. 2020; McKinnon et al. 2020).

Iapetus and Phoebe as analogs. While daytime observations were used to derive thermal inertias in the previous section, more direct methods have been used for both Iapetus and Phoebe who, at least on their surface, could be considered analogs for Arrokoth: The three bodies share similar Bond albedos (~ 0.05 Ostro et al. 2006) and Phoebe, which likely sources Iapetus’ dark side materials, may originate from the same population of KBOs as Arrokoth (Johnson & Lumine 2005; Castillo-Rogez et al. 2012)⁷. In particular, Iapetus’ leading side’s very dark top soil (especially that on Cassini Regio, CR hereafter) has been argued to be sourced from the Phoebe ring, which is itself sourced from Phoebe via micrometeorite impact gardening of its surface (Verbiscer et al. 2009). Thus considering Iapetus and Phoebe’s surface materials together as an analog for Arrokoth is not wholly unjustified, at the very least.

Based on observations made by Cassini’s Composite Infrared Spectrometer (CIRS), estimates for the thermal inertias of several of the Kronian satellites have been published (e.g., Flasar et al. 2005; Howett et al. 2010; Rivera-Valentin et al. 2011). Current thermal inertia es-

timates for Iapetus’s darkened side based on CIRS data are $6\text{ tiu} \lesssim \mathcal{I} \lesssim 21\text{ tiu}$ (Howett et al. 2010), with a more recent narrower range at $11.0\text{ tiu} \lesssim \mathcal{I} \lesssim 14.8\text{ tiu}$ (Rivera-Valentin et al. 2011). For comparison, Iapetus’ lighter trailing side surface materials is modeled from CIRS data to have $12\text{ tiu} \lesssim \mathcal{I} \lesssim 33\text{ tiu}$ (Howett et al. 2010), and possibly more tightly constrained at $15\text{ tiu} \lesssim \mathcal{I} \lesssim 25\text{ tiu}$ (Rivera-Valentin et al. 2011). Analysis of CIRS data provides estimates for Phoebe’s surface thermal inertias around $\mathcal{I} = 30\text{tiu}$ (Spencer et al. 2004; Flasar et al. 2005).

It is also important to note that based on thermal modeling leveraged against Cassini RADAR data, which was used to observe CR’s subsurface at 2.2 cm, Le Gall et al. (2014), report higher thermal inertias of at least around $\mathcal{I} \approx 50\text{ tiu}$ and possibly even $\mathcal{I} > 200\text{ tiu}$. Given that the electric skin-depths in the radio are vastly larger than in the infrared, this higher \mathcal{I} estimate is likely characteristic of surface materials far deeper than 20cm. Given the likelihood that this deeper (presumably) H_2O ice is both compacted and in cubic crystalline form, we do not consider it as a plausible analog for Arrokoth (see further below).

The thermal inertia of amorphous H_2O ice grains. Even though New Horizons did not directly detect H_2O ice on Arrokoth’s surface, theoretical considerations including global disk evolution modeling indicate that planetesimals formed out beyond the water snowline should be made up of significant amounts either H_2O ice grains or more complex silicate grains with H_2O locked in within them (e.g., Estrada et al. 2016, and many others). Perhaps for Arrokoth these H_2O ice grains are encased by a thin cover of methanol or other hydrocarbons. Moreover, a recent study of the carbonaceous chondrites NWA5717 and Allende (Simon et al. 2018) reveal that these primitive bodies are comprised of cm-scale aggregates of sub-mm chondrules (with average diameters of the distribution mode in the range 0.15-0.70 mm). These authors find that a variety of sub-groups of particles (characterized by different compositions and/or lithologies) manifest similar size distributions and aggregate character, which lead them to posit that the same size sorting process might be operating across the entire early planetesimal formation phase of the solar nebula.

These considerations taken together lead to the not-unreasonable proposal that small KBO bodies like Arrokoth are composed of fluffy aggregates of H_2O - dominated sub-mm particles. Assuming H_2O to be the dominant component of individual grains and assuming that the grains were assembled into Arrokoth in situ, then it is also not unreasonable to propose that they

⁷ Although recent challenges to this view have been raised based on the similarities of Phoebe’s spectral properties to the C-type class of asteroids (Hartmann 1987; Matson et al. 2009), as well as open questions based on internal thermal evolution modeling of its early history (Castillo-Rogez et al. 2019).

are and have always been in an amorphous crystalline form. This is particularly compelling since the amorphous to cubic crystalline transition in type 1h H₂O ice becomes important on the timescale of the solar system’s existence once temperatures exceed 70K (Efimov et al. 2011) – a condition unlikely to have been possible at 40-45 AU where CCKBOs reside. For reference we note that amorphous H₂O ice has a thermal conductivity that is lower than its cubic-phase counterpart by an order of magnitude or more when compared under the same thermophysical conditions (Andersson & Suga 1994).

Motivated by a need to explain Mimas’ estimated thermal inertia Ferrari & Lucas (2016) have suggested that the low \mathcal{I} observed of a large array outer-solar system bodies (Centaur, TNOs, etc.) might be rationalized as arising from primitive highly porous grains of amorphous H₂O ice grains. We entertain this possibility for Arrokoth starting with a brief theoretical primer on the matter following Ferrari & Lucas (2016):

On an airless body, the effective thermal inertia of a fluffy aggregate of icy-particles of size R_g and intrinsic ice-grain density ρ_{ice} is posited in the form

$$\mathcal{I} = \sqrt{(1-p)\rho_{\text{ice}}C_p(T)(K_r + K_c)}, \quad (35)$$

The effective conductivity, $K_{\text{eff}} \equiv K_r + K_c$, is the sum of the grain-to-grain heat transport via radiation (K_r) and the thermal conduction from grain to grain across shared contact points (K_c). For K_r there are several known approaches (e.g., Shoshany et al. 2002; Piqueux & Christensen 2009) but here we adopt the physically tractable model form of Gundlach & Blum (2012) where

$$K_r = 8\epsilon\sigma T^3 R_g \phi_r(p), \quad \phi_r(p) \equiv \frac{\epsilon_1 p}{1-p}, \quad (36)$$

where ϵ is the IR emissivity. Grossly speaking, the expression represents the transport of blackbody radiative energy across the chasm separating grains of similar size (i.e., $\sim R_g$). The porosity dependent radiation exchange factor $\phi_r(p)$ accounts for the added effective distance this radiation must travel due to increasingly rarefied interstitial structure of low porosity grain aggregates. $\epsilon_1 = 1.34$ is a structural constant of the model.

The contact mitigated conductivity can be described with Johnson–Kendall–Roberts theory of contact mechanics (JKR hereafter, Johnson et al. 1971),

$$K_C = h\phi_c(p)K_A, \quad (37)$$

where $\phi_c(p)$ is another porosity dependent factor taking into account reduced conduction due to the increase of vacuum space as p approaches 1. Here we assume

the form $\phi_c(p) = 2(1-p)$, which is an averaged approximation based on empirical data across a range of porosities as reported in Gusarov et al. (2003) (also see Ferrari & Lucas 2016). K_A is the intrinsic conductivity of an amorphous H₂O ice grain that can be estimated on theoretical grounds to be given by

$$K_A = C_p \rho_{\text{ice}} v_{\text{ph}} \lambda_{\text{mol}} / 4, \quad (38)$$

where v_{ph} is its phonon speed, λ_{mol} is the typical molecule separation in the crystal. Adopting this theoretical estimate checks out well against experimental data at temperatures slightly higher than that of interest here (~ 70 K, Andersson & Suga 1994). Absent experimental verification in the colder temperature range relevant here, we assume Eq. (38) is valid for our purposes. We treat H₂O ice’s heat capacity – which is assumed to be the same in its cubic crystalline and amorphous forms – according to its known temperature dependence, for which Shulman (2004) has developed an empirical form for based on experimental data in the range of 0 and 273K (see Eq. 4 of Shulman 2004). The Shulman approximation is an improvement over the often used one attributed to Klinger (1980), in which $C_p(T) = 7.49(T/1\text{K}) + 90$ J/m/kg.

The grain-grain contact radius a reflects the elastic deformation resulting from adhesive “pinching” forces related to a grain’s intrinsic surface tension plus the deformation that occurs under a given load. For the kinds of low gravities of concern here, it is expected that adhesive forces will dominate overburden load down to at least a few meters on Arrokoth. Thus for amorphous water ice grains under negligible load the Hertz factor simplifies to

$$h = \frac{a}{R_g} = \left(\frac{L_{\text{ec}}}{R_g}\right)^{1/3}, \quad L_{\text{ec}} \equiv \frac{9\pi(1-\nu_p^2)\gamma}{4E}, \quad (39)$$

where E is the ice grain’s Young’s modulus, ν_p is the Poisson ratio, and γ is the ice grain’s surface tension. The elastocapillary length scale L_{ec} nominally denotes deformation scale at which restorative elastic forces balance adhesive ones arising from surface tension (e.g., Jagota et al. 2012; Style et al. 2013).

Fig. 19 shows theoretical predictions of \mathcal{I} for several values of porosity in which $\epsilon = \epsilon_{\text{IR}} = 0.9$ with additional parameter inputs found in Table 6.1.3. For putative grain sizes $0.1\text{mm} < R_g < 1\text{mm}$ and temperature range $20\text{K} < T < 50\text{K}$, the thermal inertia of amorphous H₂O ice with $p = 0.6$ broadly falls into the range $5 \text{ tiu} < \mathcal{I} < 25 \text{ tiu}$, while for $p = 0.8$ \mathcal{I} it lies within $2 \text{ tiu} < \mathcal{I} < 12 \text{ tiu}$.

These figures also show that for a given T and p there are values of R_g where \mathcal{I} is minimized. This is easy to

Table 3. Various thermophysical and related quantities for amorphous H₂O ice.

Quantity	Value	Note
E	$\sim 2.4 \times 10^{10}$ Pa	near $T = 50$ K
ν_p	0.33	
γ	0.07-0.37 J/m ²	range of measurements
ρ_{ice}	940 kg/m ³	
v_{ph}	2500 m/s	
λ_{mol}	5×10^{-10} m	

For source references see [Ferrari & Lucas \(2016\)](#).

understand as the radiative conductivity K_r has a linear dependence on R_g while the contact limited ice conductivity K_C diminishes as $R_g^{-1/3}$: the former becomes more efficient as radiation travels across longer distances in the matrix as R_g increases while for fixed L_{ec} the latter becomes more effective because smaller grain sizes means that grain-grain contact area approaches the surface area of the grains themselves (i.e., $h \rightarrow 1$). This means that for given inputs (T, p , etc.) that $\mathcal{I} \geq \mathcal{I}_m$, where

$$\mathcal{I}_m = 1.325 \left[(1-p) C_p \rho_{ice} \left(8\epsilon\sigma T^3 K_A^3 L_{ec} \phi_r \phi_c^3 \right)^{1/4} \right]^{1/2}, \quad (40)$$

at corresponding grain size $R_g = R_m$

$$R_m = \left(\frac{L_{ec}^{1/3} \phi_c K_A}{24\epsilon\sigma \phi_r T^3} \right)^{3/4}. \quad (41)$$

The numerical factor on \mathcal{I}_m comes from the minimization procedure and is an approximation to $\sqrt{3^{1/4} + 3^{-3/4}}$. As can be gleaned from Fig. 19 we note that these extreme values occur for grain sizes of interest based on origins considerations (sub-to-few mm size) within the range of plausible ice porosities relevant for Arrokoth ($0.6 < p < 0.8$). Fig. 20 shows $\mathcal{I}_m(T, p)$, and we observe that the for the relevant temperature and porosity ranges, $\mathcal{I} \leq \mathcal{I}_m \approx 1$ -5 tiu are not possible, thus forming a reasonable lower bound for \mathcal{I} . We also observe from the form of R_m in Eq. (41), as well as from scanning the solutions shown in Fig. 19, that \mathcal{I}_m achieves its minimum in the 20-50 K temperature range for grain sizes between $0.7\text{mm} < R_g < 5\text{mm}$.

6.1.4. A speculative synthesis

Despite the analysis of the previous sections, we can at best offer likely possible candidates for Arrokoth's near surface materials that are consistent with the $T_{b,obs} = 29 \pm 5\text{K}$ measurement made by the REX instrument. This speculation is proffered on the basis of certain uncontroversially sober assumptions that: (1) Arrokoth's

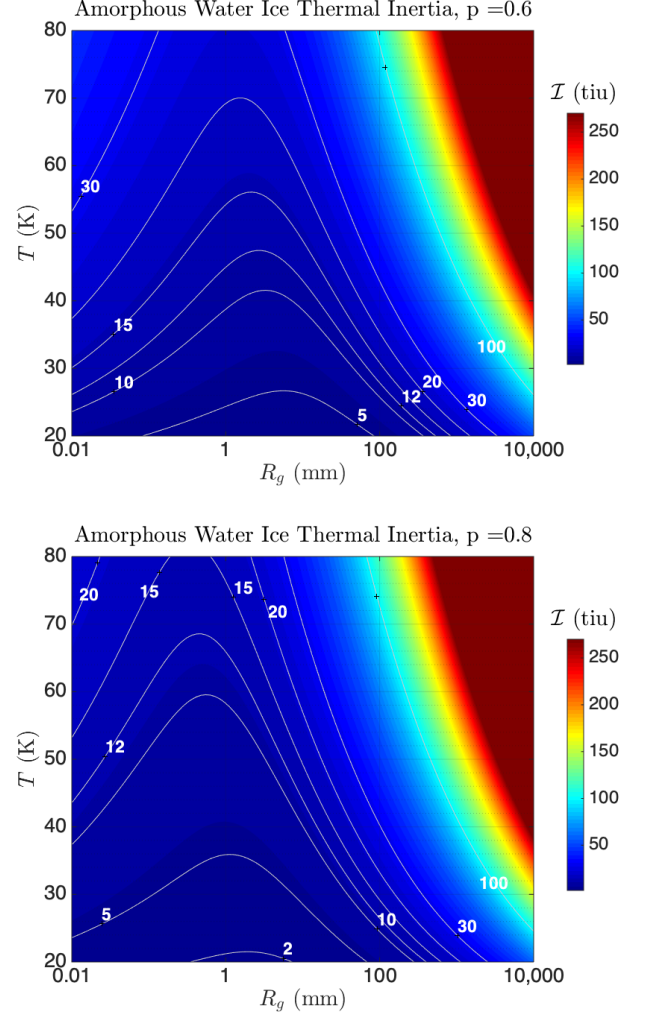


Figure 19. Predicted thermal inertia of amorphous ice as a function of grain size and temperature for two porosities: (top) $p = 0.6$, (bottom) $p = 0.8$ and $\gamma = 0.37\text{J/m}^2$ and $\epsilon = \epsilon_{IR} = 0.9$. White contours highlight key \mathcal{I} values for reference

surface materials and/or layers are uncompacted retaining a porosity in the range $0.6 < p < 0.8$ consistent with Arrokoth's mean density $\sim 250 - 350 \text{ kg/m}^3$ – on the assumption that its constituent grains are typical of the mean densities of relaxed KBOs ($\sim 1600 \text{ kg/m}^3$, e.g., [Castillo-Rogez et al. 2012](#); [Bierson & Nimmo 2019](#)); (2) As being a member of the CCKBOs, Arrokoth's surface temperature probably never exceeded 70 K at any time during its natural history owing to its stable location in the Kuiper Belt; (3) the X-band value of the imaginary part of the dielectric permittivity of Arrokoth's subsurface materials is no less than that of unpolluted H₂O ice, i.e., $\epsilon'' > 10^{-4}$.

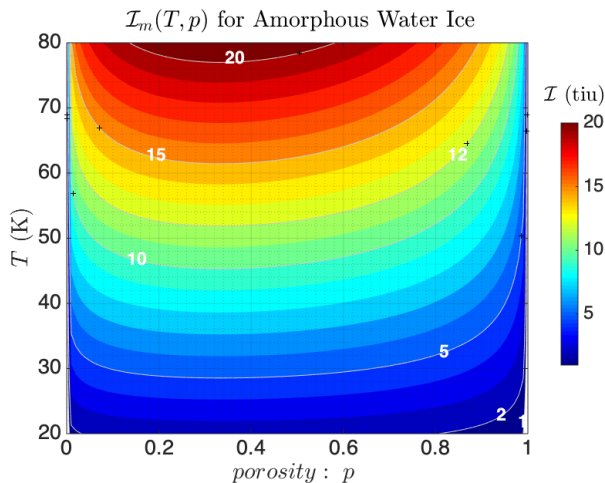


Figure 20. Minimum thermal inertia for amorphous H₂O ice as a function of T and p with $\epsilon = 0.9$. Under given conditions this quantity implies that $\mathcal{I} \geq \mathcal{I}_m(T, p)$. Note also this quantity is extremized at around $p \approx 0.32$.

By analogy to Phoebe and Iapetus’ leading side’s dark materials – mainly owing to their shared low albedos – we favor the assumption that Arrokoth’s X-band emissivity is in the range $\langle E_{\text{eff}} \rangle = 0.9 - 1$. We rule out $\langle E_{\text{eff}} \rangle$ values of 0.7 on the basis that it would correspond to ice with ϵ'' well below 10^{-4} . We deem $\langle E_{\text{eff}} \rangle = 0.8$ unlikely for similar reasons on the low \mathcal{I} end (< 20 tiu). $\langle E_{\text{eff}} \rangle = 0.8$ seems unlikely on the high \mathcal{I} end (> 80 tiu) despite its being a possible solution (e.g., see Fig. 16) as it would correspond to \mathcal{I} for either very low or very high porosity H₂O ice (both amorphous or cubic). According to Fig. 19 the high porosity ice grain solution that predicts $\mathcal{I} > 50$ tiu would correspond to boulder sized solid ice grains, which is difficult to produce if the grains are formed during the era of planetesimal formation (e.g., Estrada et al. 2016). The low porosity ice grain solution that yields such high thermal inertias would correspond to sub-micron sized amorphous H₂O ice grains that, while possible, is hard to reconcile with the meteoritic record and planetesimal formation models.

If Arrokoth’s subsurface materials are composed mainly of mm-scale amorphous H₂O ice grains, then its thermal inertia is likely below 10-20 tiu since higher thermal inertias are not reasonable to expect for amorphous H₂O ice at the porosities of interest here. Of course, thermal inertias in the range 50-100 tiu are possible, but only if the H₂O ice is in cubic form, which is a possibility only if the near surface materials have experienced sustained periods with temperatures higher than 70-80 K (see extensive discussion in Ferrari & Lucas

2016). As mentioned above, high values of \mathcal{I} are possible for amorphous ice if the grains are like boulders in size where thermal transport is governed by radiation, but such large constituent surface material is hard to justify from an origins perspective. The same theoretical concerns suggest that Arrokoth’s thermal inertias are no less than 2 – 5 tiu, thus forming a reasonable lower bound for \mathcal{I} as lower values are not predicted for amorphous H₂O ice with porosities $0.6 < p < 0.8$.

Taken together we see from inspecting the low ϵ' column of Fig. 16 corresponding to its first two rows ($\langle E_{\text{eff}} \rangle = 0.9, 1.0$) that for $1 \text{ tiu} < \mathcal{I} < 10 \text{ tiu}$, the $T_{\text{b,obs}} = 29 \pm 5 \text{ K}$ prediction occurs in the range $10^{-4} < \epsilon' \lesssim 10^{-2}$, which is consistent with permittivity values for H₂O ice in the GHz range as briefly surveyed in section 6.1.1 and discussed further in Bird et al. (2022). Amorphous H₂O ice of mm-scale is therefore a strong candidate material to account for the Arrokoth’s subsurface materials.

However, the same solution survey cannot rule out tholins – hydrocarbons produced from plasma discharging in mixtures of methane and nitrogen – as candidate materials as they are expected to be ubiquitous reddening agents of the outer solar system (Cruikshank et al. 2005a). Consideration of laboratory data of tholins summarized in section 6.1.1 as well as in Bird et al. (2022) indicates that high porosity tholins exhibit $10^{-4} < \epsilon' \lesssim 10^{-3}$, which is also consistent with $T_{\text{b,obs}}$ for both $\langle E_{\text{eff}} \rangle = 0.9, 1.0$. Unfortunately, thermal inertias for tholins are not well constrained and while the $T_{\text{b,obs}}$ measurement is consistent with the permitted range of thermal inertias for amorphous H₂O ice (i.e., 1-20 tiu) for $\langle E_{\text{eff}} \rangle = 1.0$, the full range of thermal inertias are permitted for $T_{\text{b,obs}}$ in the case where $\langle E_{\text{eff}} \rangle = 0.9$ (second row of Fig. 16). We suspect that the surface ice is likely an admixture of amorphous H₂O ice and tholins, with the latter forming a small percentage of the composite, much in line with suggestions made for the make-up of the Kronian satellites (Cruikshank et al. 2005b). If the dominant constituent is the H₂O component, then we suspect the lower range of permissible thermal inertias characterizes the $\langle E_{\text{eff}} \rangle = 0.9$ case too.

We observe that in the recent study by Ferrari et al. (2021), where they examined the thermal response of the Kronian moons – but not including Iapetus and Phoebe – that a nominal upper bound conductivity of $K_{e0} \sim 0.001 \text{ W/m/K}$ was adopted for their model tholin-covered amorphous H₂O ice grains. If such a tholin-H₂O ice complex were present on Arrokoth, it would correspond to an upper bound value $\sqrt{(1-p)\rho_{\text{ice}}K_{e0}} \approx 11$ tiu.

6.2. On the comparison between simple theory and full results

In Section 2 we constructed a simplified algebraic theory for the predicted temperatures on the winter and summer sides. It is of interest to see how well this theory works against our predictions based on the more detailed sophisticated model we have developed here. Examining Fig. 5 shows that at encounter day Arrokoth was in its late southern hemisphere spring phase of its orbit. Given that it was near the southern summer solstice, it is useful to compare the distribution of the predicted encounter day surface temperatures against the simplified theory of Sec. 2. In Fig. 21 we re-plot the surface temperature distribution shown in the first panel of Fig. 7, where we have distinguished between surface facets in the polar and tropical zones. Surface facets are designated as belonging to the polar zone if there exists at least one Arrokoth day in which the sun never rises, while tropical zones are those facets in which the sun rises daily. The distribution shows two modes. The low end mode corresponds to approximately 12.5K, which is the predicted value for $T_{s,w} \approx 12.2\text{K}$ based on the results shown in Fig. 2 for $\mathcal{I} \approx 2.54$ tiu (the low end of likely \mathcal{I} values as discussed in the previous section). The high temperature mode shows that the peak temperature sits at around 58.5K. The simple theory predicts a typical summer time temperature of $T_{s,s} \approx 60\text{K}$, which is only slightly higher than high end mode seen in the distribution, and where this discrepancy is likely due to comparing the simple theory against a solution for a time slightly shy of solstice (cf., Fig. 5). We conclude that the simple theory of Sec. 2 is overall useful especially with respect to predicting the temperatures on both the summer and winter sides near around solstice.

6.3. On the value the time-asymptotic solution method

The traditional approach to solving Eqs. (13-15), while similarly involves precomputing the shape model analysis and insolation profile, calls for developing an initial value solution to Eq. (13). Accurately forward time evolving the heat equation can be treacherous and often time-consuming, especially if the parameters of the problem make the system numerically stiff (requiring short time-stepping), although there are many recent methods developed in the astrophysical literature that alleviate this computational overhead while preserving accuracy and stability in various problems involving diffusion operators (e.g., Meyer et al. 2012).

The main issue, however, is developing a solution to a periodically driven problem that is “time-asymptotic”, in the sense that the long-time state of the system – certainly after tens of millions of orbits since formation

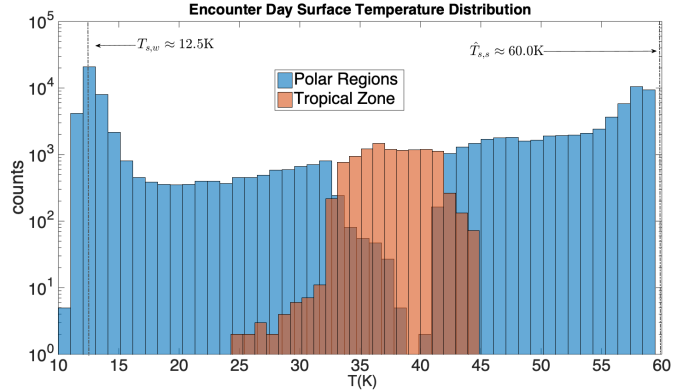


Figure 21. A more detailed view of encounter day surface temperatures. Comparisons between simple theory predictions are shown: vertical line at $T \sim 60\text{K}$ corresponds to the “summer” side predictions of the simple theory while the vertical line at $T \sim 12.5\text{K}$ corresponds to the “winter” side predictions of the same.

(McKinnon et al. 2020) – is also periodic with the external driver’s periodicity (if, however, out of phase, etc.). Arrokoth is likely in such a time-asymptotic state given that its orbital elements are not thought to have experienced strong chaotic or aperiodic episodes, at least not in recent history (Porter et al. 2018). Thus, the problem we have here lies in initiating the initial value problem with the right initial data that sets the solution off into an exactly periodic transient-free state. But this is something which, in general, is not known *a priori*. In practice, such initial value problems are setup up with some initial profile (satisfying boundary conditions), and subsequently forward evolved until the time-periodic asymptotic state is eventually reached. But this may take time to achieve (sometimes dozens of forcing periods), which can be expensive. The Fourier transform method utilized here, as well as in Titus & Cushing (2012); White et al. (2016), while slightly costly due to the fast Fourier transform itself, immediately admits an exactly periodic solution, with no transient structure. There is no forward time stepping involved and the resulting solutions are accurate to spectral precision, which makes this solution method attractive from the standpoint of generating reliable solutions.

6.4. On thermally driven mechanical erosion, a speculation

Beyond circumstantial evidence for methanol based on spectral fitting to LEISA data obtained by New Horizons (Stern et al. 2019; Grundy et al. 2020), what are Arrokoth’s near surface materials and what are their thermo-mechanical properties remains unknown to date.

Based on surveys of other CCKBOs (Lellouch et al. 2013) only bulk thermal inertias probing diurnal skin depths are reasonably known. For the solutions displayed in Section we have adopted a representative value of $\mathcal{I} \approx 2.5$ tiu, but we keep in mind that these values may be larger based on the discussion found in section 6.1.

Nevertheless, these thermal solutions with relatively low values of \mathcal{I} might suggest something about Arrokoth’s erosive character. Erosion driven by thermal cycling – wherein cracks nucleate and grow due to a material’s non-zero coefficient of thermal expansion – might be a relevant effect on Arrokoth over the course of its natural history. Such a process has been hypothesized in order to explain the nature and origin of erosion on for cometary bodies (e.g., for 67P/Churyumov-Gerasimenko, Attree et al. 2018).

We focus here on thermomechanical erosion and do not consider thermal erosion driven by sublimation since volatile ices are neither known to be present on Arrokoth’s surface nor would be expected to be extant there (see previous section). Among other things, however, estimating actual rates of erosion requires knowing what is the local temperature temporal profile, the materials coefficient of thermal expansion, its effective porosity, Young’s modulus, Poisson’s ratio, and if the thermal cycling is on a long enough timescale, its viscous relaxation properties like the materials activation energy (Mellon 1997; Molaro et al. 2015, see latter reference for a recent comprehensive discussion). Nevertheless, we speculate upon the relative amount of thermally driven mechanical erosion *over the course of one orbital time* assuming the near surface of the body is uniformly composed. Fig. 11 indicates that the highest minimum temperature ($\sim 20 - 30$ K) over the course of one orbit occurs along a narrow line of surface located within the tropical zone and, moreover, appears to trace along the rims of putative craters or depressions found in that region. The implied extreme temperature variation is shown in Fig. 13, which shows for each facet the difference of the maximum and minimum temperatures achieved over the course of one orbit, i.e.,

$$\Delta T_i \equiv \max(T_i) - \min(T_i). \quad (42)$$

The figure indicates that the bulk of the polar regions experiences ΔT_i close to 50 K, while the tropical zones experience ΔT_i closer to 30K. The aforementioned narrow line within the tropical zone has a temperature variation of about only 10K. With all other variables held fixed, it stands to reason that the thermal erosion is greatest across the polar regions where ΔT_i is large, and significantly weakens upon entry into the tropical zone and

even further weakens as one approaches the narrow line of real estate within in which $\Delta T_i \approx 15 - 20$ K. While this relative prediction is reasonable, the actual amount of erosion that has taken place over Arrokoth’s natural history cannot be ascertained until the actual composition of its surface materials are unambiguously determined, together with information about their thermal and viscoelastic properties, with particular attention to its rheology.

As a final remark, we note that the thermal driving is likely most extreme on Arrokoth’s equatorial latitudes during its equinoxes since these regions are getting extreme illumination variations on the the short 15.9 hour diurnal period P_{day} ($\omega_{\text{day}} = 2\pi/P_{\text{day}}$). But the thermomechanically driven erosion taking place on this short timescale is also restricted to the upper 1-2mm of surface since the thermal wave lengthscale ℓ_{day} is shortened by comparison to ℓ_{orb} (≈ 1 m) by a factor of $\sqrt{\omega_{\text{orb}}/\omega_{\text{day}}} \approx 1/400$.

6.5. Other Various Caveats

Despite the intrinsic scientific value of these solutions, several aspects of the thermal model method utilized here could be improvement. We acknowledge a few here with the aims of developing even more refined solutions in the future. We have assumed the thermal inertia (and by implication, the thermal conductivity) is a constant independent of temperature and porosity. Indeed the time-asymptotic method we have employed relies on this feature, which permits using fast Fourier transform techniques to develop solutions (Titus & Cushing 2012; Schloerb et al. 2015; White et al. 2016). However, although not done here, a temperature dependence of the thermal inertia may be formally built into the method at the cost of added iterations to the solution process – a matter we will develop further with future follow-up work. We have also assumed constant stratigraphy and/or subsurface porosity, which could also be unrealistic. But similar to our point above this can be similarly remedied by iteration or by directly building stratigraphy into the solution itself. We demonstrate how this is done in Appendix C where we develop a subsurface thermal solution for a material composed of two different conductivities where the transition occurs h meters below the surface. The solution may be developed analytically, as was done for the discussion in the text, and coded directly into the thermal solver. This procedure naturally generalizes to multiple layers with differing properties.

6.5.1. On the use of a single albedo value

New Horizons imaging showed the existence of several bright rings and patches painting its surface (e.g.,

see the bright patches in Fig. 4, also see [Spencer et al. 2020](#)), with normal reflectances of these bright patches being about twice that of the rest of the terrain. Given that these images were taken at high solar phase angle, the observed relatively enhanced brightness in these regions is likely “the result of the extreme illumination conditions rather than the intrinsic albedo of the surface,” ([Stern et al. 2021](#)). In light of this and in addition to determining Arrokoth’s mean hemispherical albedo, [Hofgartner et al. \(2021\)](#) have produced an albedo map of the closest approach image (see their Fig. 4) in which the bright patches are assessed to have albedos as high as 0.09. Provided all other thermophysical properties are the same across bright and dark patches, we find that the temperatures in these bright regions are overestimated by less than 0.5K: if T_{dark} is the estimated temperature of the bright terrain assuming the lower albedo ($A_{\text{dark}} = 0.063$) and $T_{\text{bright}} \equiv T_{\text{dark}} - \delta T$ would be its true correct value based on ($A_{\text{bright}} = 0.09$), where δT is the correction factor, then

$$\left(\frac{T_{\text{dark}} - \delta T}{T_{\text{dark}}}\right)^4 = \frac{1 - A_{\text{dark}}}{1 - A_{\text{bright}}}, \quad (43)$$

predicting $\delta T/T_{\text{dark}} \approx 0.007$, which for $T_{\text{dark}} \approx 60\text{K}$ amounts to $\delta T = 0.42\text{K}$.

6.5.2. On the neglect of reflected light

In our calculations we have included thermal IR in the re-radiation calculation and neglected reflected light. This neglect has minor consequences on the final determined temperatures following the same line of thinking as above, where we find the error is even weaker. If we treat the reflected light as a Lambertian process, then the light received at a given facet will be traced by the IR re-radiated light from all other facets. We showed earlier that for a given facet i the energy received from all other facets ($f_{i,\text{rr}}$) amounts to about 10 percent of the locally absorbed solar insolation ($f_{i,\odot}$), i.e., $f_{i,\text{rr}} \approx \chi f_{i,\odot}$, where $\chi \leq 0.1$. We can estimate the amount of reflected light neglected in this accounting to be about $A f_{i,\text{rr}}$, such that the correct amount of light received from the surrounding landscape is better estimated by $\tilde{f}_{i,\text{rr}} \approx f_{i,\text{rr}}/(1 - A)$. Assuming that all other thermophysical properties remain the same, the correct temperature $T_{i,\text{cor}} = T_i + \delta T$ compares to the estimated temperature T_i via the same Stefan-Boltzmann law argument applied in the previous section with

$$\left(\frac{T_i + \delta T_i}{T_i}\right)^4 = \frac{f_{i,\odot} + f_{i,\text{rr}}}{f_{i,\odot} + \tilde{f}_{i,\text{rr}}} = \frac{1 + \chi}{1 + \frac{\chi}{1 - A}}, \quad (44)$$

which, given our estimate for χ , means $\delta T_i/T_i \approx 0.0016$, which for $T_i \approx 60\text{K}$, implies that neglecting reflected

light on Arrokoth amounts to underestimating the local temperature by $\delta T_i \approx 0.1\text{K}$. In summary it is conceivable that Arrokoth is close to a blackbody, i.e., one that is marginally reflective and radiating most of its heat in IR.

6.5.3. On the expiration of surface N_2 ice on Arrokoth

We can ask about the fate of volatile ices like N_2 and CO (with similar properties) on an airless body like Arrokoth following some of the thinking used to address similar concerns about the nature of Oumua-mua ([Jackson & Desch 2021](#)). With typical solar insolation values based on Arrokoth’s semimajor axis, i.e., $\tilde{f}_{\odot} \approx 0.7 \text{ W/m}^2$, a vacuum exposed surface layer of N_2 ice on Arrokoth would sublime at a rate of $3.5\text{m}^3/\text{orbit}$. This conservative figure derives from assuming an N_2 ice albedo of $A = 0.9$ (i.e., based on Pluto observations, [Grundy et al. 2016](#); [Schmitt et al. 2017](#)) and an enthalpy of N_2 sublimation $\mathcal{L} = 225\text{kJ/kg}$ that, if we assume a surface layer of N_2 ice converts all of its received insolation into sublimation (and adjusting its temperature accordingly), would result in a mass flux $\dot{\Sigma} = (1 - A)\tilde{f}_{\odot}/\mathcal{L} = 3.4 \times 10^{-7}\text{kg/m}^2/\text{s} \approx 3.24 \times 10^3\text{kg/m}^2/\text{Arrokoth orbit}$. Under these vacuum conditions a sublimating block of ice must satisfy the relationship between mass-flux into a vacuum and a material’s vapor pressure, $P_{\text{vap}}(T)$, i.e.,

$$\dot{\Sigma} v_k = P_{\text{vap}}(T), \quad (45)$$

(e.g., [Lebofsky 1975](#)), where v_k is the typical Boltzmann velocity. An estimate based on compiled vapor pressure data for N_2 ([Fray & Schmitt 2009](#)) shows that this balanced state is satisfied for $T \approx 27\text{K}$. Based on the shape model utilized here Arrokoth’s total surface $A_{\text{surf}} \approx 1406\text{km}^2$. Thus, if Arrokoth were uniformly covered with N_2 ice, then it would be losing a total of about 481 kg of N_2 per second $\leftrightarrow 1.6 \times 10^{28}$ particles per second, well above the mass loss rate upper limits based on New Horizons’ observation of the body ($< 10^{24}$ particles/s, [Stern et al. 2019](#)). These considerations preclude the plausibility that N_2 and CO can remain on the surface of Arrokoth for any appreciable amount of time. CH_4 , which is relatively less volatile by a factor of 10^3 (based on its vapor pressure behavior at similar temperatures) would also result in particle flux rates exceeding those observed by New Horizons. This analysis says nothing about the plausibility for reservoirs of volatile ices deep within Arrokoth. Addressing this matter requires further analysis.

7. SUMMARY

We have developed a temperature model of Arrokoth based on the 10^5 facet model published in [Spencer et al.](#)

(2020). For the bulk of the solutions displayed here, especially in Section 4, we have assumed a single value of $\mathcal{I} \approx 2.5$ tiu, together with a infrared emissivity of 0.9 and an albedo of 0.06. The choice of $\mathcal{I} \approx 2.5$ is consistent with the low end of thermal inertia values for amorphous H_2O ice as detailed at length in section 6.1. Although direct temperature measurements were not possible with New Horizons, for the day of the closest encounter we predict that the day side approach hemisphere surface temperatures were in the range of 57-60K. According to the simple model of section 2 (e.g., Fig. 2) the predicted daytime (“summer time”) surface temperature has a very weak dependence in the thermal inertia range of $1 \text{ tiu} < \mathcal{I} < 10 \text{ tiu}$. We thus expect this quoted daytime temperature range to hold for the full range of likely \mathcal{I} values. On the other hand, for the specific $\mathcal{I} = 2.5$ tiu value we predict that the obscured winter side of Arrokoth had surface temperatures in the range of 10-15K, but following the same above reasoning, based on the results shown in Fig. 2 together with the likely range for \mathcal{I} , we predict that the night side surface temperature could lie within the slightly wider range of values of 10-20K.

Arrokoth’s tropical zones receive the lowest yearly averaged insolation but exhibits the highest orbitally averaged temperatures compared to Arrokoth’s more extreme polar regions. In fact, the extreme temperature variations experienced by facets in Arrokoth’s polar zones ($\Delta T \approx 50\text{K}$) greatly exceed the corresponding variations in its equatorial zones ($\Delta T \approx 10 - 30\text{K}$). The property of our thermal model leads us to conjecture that the amount of thermal erosion in the tropical zones should be significantly lower than the erosion suffered in the polar regions.

We also find that the amount of energy received on a typical facet that is sourced from surface reradiation typically amounts to about 5% of the total irradiation, although it should be kept in mind – as a cross comparative inspection of the histograms of Fig. 7 shows – there is a spread in this figure from facet to facet, which ultimately depends upon how much of a given facet is obscured by the rest of the body. A small adopted value of \mathcal{I} means that Arrokoth’s Spencer Number is also small (≈ 0.01). In other words, this highly insulating body has very little downward directed thermal conduction from radiation received during total direct illumination (and subsequently returning it at night), amounting to about 0.5% of the typically received insolation flux budget.

Based on a generalized application of our thermal modeling we find that the brightness temperature

$T_{\text{b,obs}} = 29 \pm 5\text{K}$ measured by New Horizons’ REX instrument (Grundy et al. 2020, also see Bird et al., 2022) is consistent with porous ($0.6 < p < 0.8$) subsurface amorphous H_2O ice – possibly coated with tholins – within the thermal inertia range $1 \text{ tiu} < \mathcal{I} < 10\text{-}20 \text{ tiu}$ for given X-band emissivity $\langle E_{\text{eff}} \rangle = 1.0$. For X-band emissivity $\langle E_{\text{eff}} \rangle = 0.9$, which is similar to the low albedo (and possibly captured) KBO Phoebe, our thermal modeling predicts a wider range of permissible thermal inertias, with $1 \text{ tiu} < \mathcal{I} < 300 \text{ tiu}$. However the high-end of the \mathcal{I} ($> 50 \text{ tiu}$) values are disfavored for two reasons: (i) it would imply that either very large (1-10m) or very small (sub-micron) amorphous H_2O ice grains are dominant constituents of Arrokoth’s near surface – sizes which are hard to reconcile from an origins planetesimal formation perspective – and, (ii) it might imply that the near surface H_2O ice grains are in cubic crystalline form, but this would mean that Arrokoth’s surface experienced sustained periods of relatively elevated temperatures exceeding 70K (corresponding to the amorphous-cubic transition occurring on times shorter than Arrokoth’s natural age). Such high thermal inertias might be characteristic of low-porosity tholins, but that is currently unknown and remains to be more completely studied under relevant laboratory conditions.

As such we favor the interpretation that the REX $T_{\text{b,obs}}$ measurement indicates that Arrokoth harbours porous hydrocarbon-coated amorphous H_2O ice grains of rough size $\sim 0.1 - 1\text{mm}$, with $1 \text{ tiu} < \mathcal{I} < 10\text{-}20 \text{ tiu}$, and characterized by an X-band emissivity in the range 0.9 and 1.

Acknowledgements. O.M.U. and the rest of the New Horizons team acknowledge support from the New Horizons Kuiper Belt Extended Mission grant for support in producing this work. J.T.K. acknowledges that portion of the research was carried out at the Jet Propulsion Laboratory, California Institute of Technology, under a contract with the National Aeronautics and Space Administration (80NM0018D0004). J.T.K. also acknowledges supported by the California Institute of Technology Joint Center for Planetary Astronomy postdoctoral fellowship. O.M.U. acknowledges fruitful conversations with A. Jindal and A. Hayes (Cornell University). We are indebted to insights shared with us by B. Butler (NRAO) and M.A. Gurwell (CFA). The authors acknowledge and are grateful for the helpful comments made by the two reviewers of the manuscript.

A. DETAILS OF SHAPE ANALYSIS OF SECTION 3.2

This section is concerned with determining how much a given piece of landscape is visible to the rest of the landscape (a “who-sees-who” list), and is meant to address how the integral expression in Eq. (15) is calculated. The considerations here reference Fig. 22. Each facet i has an outwardly pointing normal $\hat{\mathbf{n}}_i$ and associated surface area s_i such that $d\hat{\mathbf{s}}_i = s_i \hat{\mathbf{n}}_i$. Our goal is to determine which facets j are visible to facet i . This involves ruling out all (1) facets j whose unit normals $\hat{\mathbf{n}}_j$ face away from facet i , (2) rejecting all facets j that are below the facet i ’s horizon, and finally (3) discarding all facets j that are blocked by intervening facets. We treat each of these in order:

We first determine a separation vector $\mathbf{r}_{ij} = \mathbf{r}_j - \mathbf{r}_i$, and further parse this in terms of a scalar and unit vector $\mathbf{r}_{ij} = r_{ij} \hat{\mathbf{m}}_{ij}$, in which $r_{ij} = |\mathbf{r}_{ij}|$ and $\hat{\mathbf{m}}_{ij}$ is a unit vector pointing from the center of facet i to the center of facet j : (1) a facet j is deemed below the horizon if $\cos \theta_i = \hat{\mathbf{m}}_{ij} \cdot \hat{\mathbf{n}}_i < 0$, (2) a facet j is pointed away if $\hat{\mathbf{m}}_{ij} \cdot \hat{\mathbf{n}}_j > 0$, for which we define $\cos \theta_j \equiv -\hat{\mathbf{m}}_{ij} \cdot \hat{\mathbf{n}}_j$. Therefore in order for a facet j to be a candidate for visibility by facet i , both $\cos \theta_i > 0$ and $\cos \theta_j > 0$. It then follows that all candidate facets j passing the above two criteria are tested for actual visibility using a ray-tracing routine. The prototype code we have built is run on Matlab 2014a and we have therefore used a community wide tested ray-tracing Matlab routine called `inpolyhedron`, which ascertains whether not elements of a given ray of points are inside a closed surface.

For all the facets j visible to facet i , we determine the local altitude of the highest visible facet by identifying for which facet j is $\cos \theta_i$ maximum, and we assign the value of this special altitude $\beta_i = \pi/2 - \theta_i(\max)$. This information is used in speeding up the solar insolation calculation of the next section. In some notable instances a given facet i sees no other facets of the body, in which case its $\beta_i = 0$.

The luminosity apparent to facet i of a *visible* flat Lambertian facet j , with area s_j and inclined at an angle $\cos \theta_j$, emitting with a flux f_j is $f_j s_j \cos \theta_j$. Defining F_{ij} as the flux absorbed by facet i from facet j , it follows that

$$F_{ij} = f_j K_{ij}, \quad K_{ij} = \frac{s_j \cos \theta_j \cos \theta_i}{2\pi r_{ij}^2}, \quad (\text{A1})$$

where the factor 2π accounts for the fact that emitted radiation spreads out only across 2π steradians. We note that the expression in Eq. (A1) likely badly quantifies the received irradiation from (say) neighboring facets especially if the angles formed between their planes of intersection are highly acute. This problem would be especially acute if the quality of the local topography *on the scales of interest* appeared to be fractal. This is not the case here. By identifying $f_j = \varepsilon \sigma T_j^4$, then it also follows that the body integral term in Eq. (15) becomes

$$\int_{\partial S} f_j S_{ij} d\hat{\mathbf{s}}_j \rightarrow \sum_{\forall j \text{ visible}} f_j K_{ij}, \quad (\text{A2})$$

where, by implication, $S_{ij} d\hat{\mathbf{s}}_j \rightarrow K_{ij}$. In practice K_{ij} is constructed as a sparse matrix in which the column elements j are non-zero for those facets that are visible to i . By its construction a given facet is not visible to itself, therefore $K_{ii} = 0$. Finally, we note that although this analysis is expensive (~ 5 hours when run as a parallel computation on a 4-core 3.1 GHz Intel system), it is only done once for a given *static* shape model. All other calculations, including parameter studies and so forth that are done hereafter, utilize K_{ij} .

In Fig. 3 we show the results of the shape analysis based on the 10^5 faceted shape model described in the previous section. The figure depicts a facet-by-facet map of the percent of open sky self-observed by Arrokoth. The percent is based on the fraction of 2π steradians occupied by other surface facets. We see how the routine identifies craters as places of relatively high obscuration ($\sim 30\%$). The neck region on the well-imaged approach trajectory (top panel) also shows similar degrees of self-obscurtion. However, the neck region on the departure trajectory, which was not directly imaged and whose structure is inferred from model fitting procedures described in [Spencer et al. \(2020\)](#) and is probably less reliable as a result, is identified as having much greater obscuration in the vicinity of $\sim 60\%$ or so. It is not a surprise given Arrokoth’s flattened structure that the relative amount of self-obscurtion is generally very weak (also see the distribution of these percentages in the first panel of Fig. 12).

B. AN EXAMPLE CALCULATION USING THE FOURIER METHOD

We detail the Fourier method solution procedure on a relatively simplified problem. We suppose we have a 1 dimensional layer with the same setup as described in the text. We imagine that the surface ($z = 0$) is illuminated

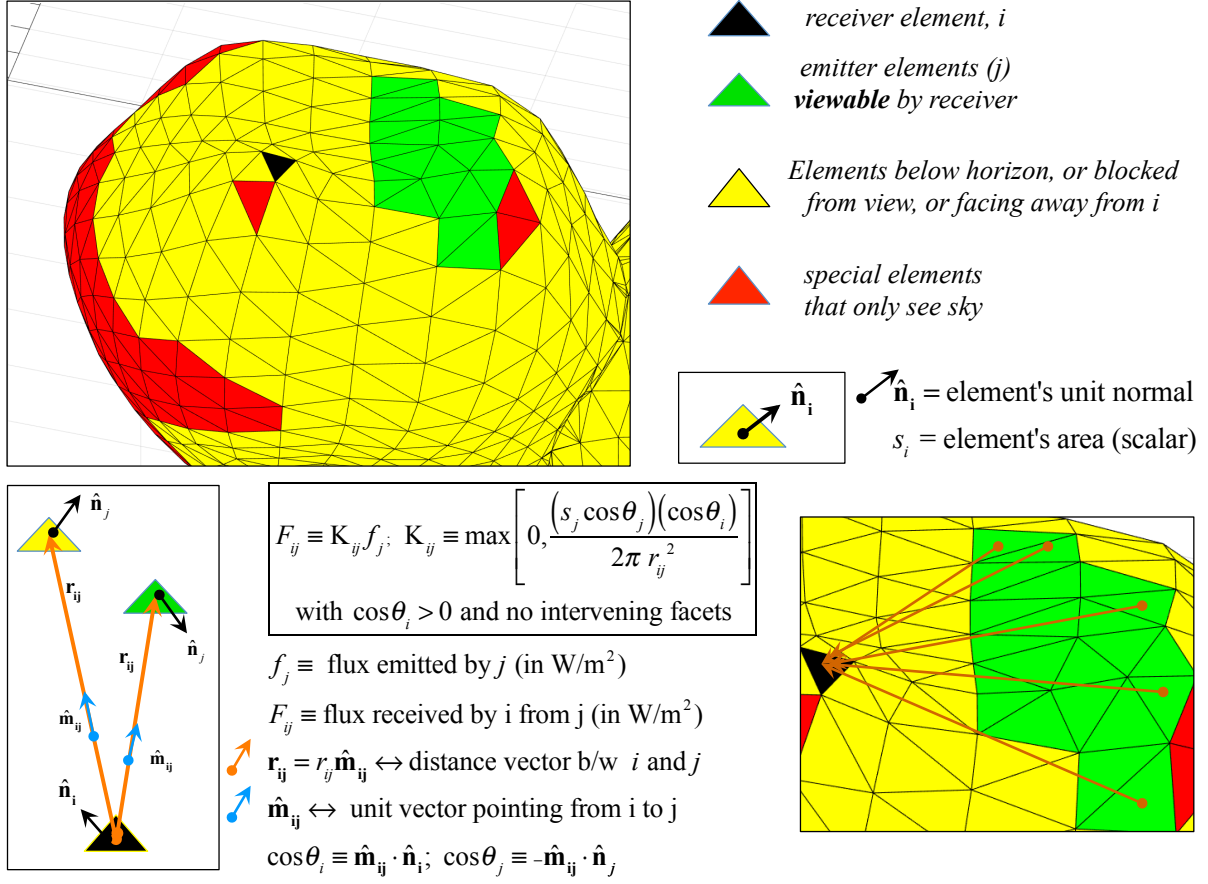


Figure 22. This diagram describes the shape analysis discussed in Section 3.2. The shape model depicted here is the low order 2000 facet model analyzed in Grundy et al. (2020). However, the methods described herein are applied to the 10^5 facet model in Spencer et al. (2020).

by a function f with period $2\pi/\omega$. The surface material's emissivity is 1. The interior temperature satisfies the heat equation

$$\rho C_p \partial_t T = K \partial_z^2 T, \quad (\text{B3})$$

The boundary conditions at the top and bottom (respectively) are

$$\sigma T^4 \Big|_{z=0} + K \partial_z T \Big|_{z=0} = f, \quad \partial_z T \Big|_{z \rightarrow \infty} = 0. \quad (\text{B4})$$

We assume all other coefficients in the above equations are constant. We represent the interior solution by a Fourier series

$$T = T_0 + \sum_{n=1}^{\infty} \Theta_n e^{k_n z - i\omega n t} + \text{c.c.}, \quad k_n = \sqrt{\rho C_p i \omega n / K}. \quad (\text{B5})$$

The above solution satisfies the heat equation for all points $z \leq 0$, including the bottom boundary condition. What remains to be determined are the coefficients Θ_n , which can be solved for by satisfying the surface boundary condition. We approach this in the following way. The vertical thermal gradient at $z = 0$ is given by

$$K \partial_z T \Big|_{z=0} = K \sum_{n=1}^{\infty} k_n \Theta_n e^{-i\omega n t} + \text{c.c.} \quad (\text{B6})$$

We can decompose the insolation forcing also as an infinite sum of Fourier harmonics, that is to say

$$f = f_0 + \sum_{n=1}^{\infty} f_n e^{-i\omega n t} + \text{c.c.} \quad (\text{B7})$$

The top boundary condition therefore becomes

$$\sigma T^4 \Big|_{z=0} - f_0 + \sum_{n=1}^{\infty} (K k_n \Theta_n - f_n) e^{-i\omega n t} + \text{c.c.} = 0, \quad (\text{B8})$$

A complete solution is had once the countably infinite number of complex valued coefficients Θ_n are determined. In practice one assumes a maximum number N of these coefficients for a sufficiently converged solution, which is assessed as such once successive changes in the final state meets some requisite set of minimum error criteria. Thus, the solution is determined for the set of Θ_n that solve Eq. (B8). Identifying the function $F(T) \equiv \sigma T^4 \Big|_{z=0}$, together with its Fourier decomposition as

$$F = F_0 + \sum_{n=1}^{\infty} F_n e^{-i\omega n t} + \text{c.c.} \quad (\text{B9})$$

we find that Eq. (B8) becomes after truncating up to N sinusoids

$$F_0 - f_0 + \sum_{n=1}^N (F_n + K k_n \Theta_n - f_n) e^{-i\omega n t} + \text{c.c.} = 0. \quad (\text{B10})$$

Taking the (fast) Fourier transform of the above yields a set of N nonlinear algebraic equations that must be simultaneously solved, namely

$$F_n(\Theta_m) + K k_n \Theta_n - f_n = 0, \quad k_0 = 0, \quad (\text{B11})$$

for each value of $n = 0, 1, \dots, N$. The term $F_n = F_n(\Theta_m)$ is a nonlinear function of all the unknown coefficients Θ_m . As such, the above set of N -coupled nonlinear equations must be solved using a Newton-Raphson (or gradient descent) type of nonlinear equation solver. In practice, this is done efficiently by assuming an initial guess for Θ_n , then backward transforming $T(z=0)$ from frequency space into temporal space, followed by calculating $F(T) = \sigma T^4 \Big|_{z=0}$, then taking F and forward (fast) Fourier transforming it into frequency space to determine each F_n , followed by assessing a solution to Eq. (B11). This usually involves an iterative procedure which requires re-executing the same set of forward-backward Fourier transform procedures to determine an improved solution, until error tolerances are met. This solution procedure is easily generalizable to nonlinear values of the conductivity coefficient K , say, which are dependent on the values of T .

C. LAYERED THERMAL SOLUTION

We suppose that the surface is composed of two layers with a transition occurring at $z = -h$ (where $h > 0$). For the sake of this illustration let us suppose that the only difference between the layers is the thermal conductivity. In keeping with our convention in the text, we set the conductivity to be K for $-h < z < 0$, and $K^{(-)}$ for $z < -h$. We therefore divide the solution to the heat equation Eq. (13) into ones appropriate to these two levels:

$$\Theta_i = \begin{cases} \sum_{n=0}^N (\Theta_{i,n} e^{k_n z} + \Xi_{i,n} e^{-k_n z}) e^{-i\omega n t} + \text{c.c.}, & -h < z \leq 0 \\ \sum_{n=0}^N \Theta_{i,n}^{(-)} e^{k_n^{(-)}(z+h)} e^{-i\omega n t} + \text{c.c.}, & z \leq -h \end{cases}, \quad (\text{C12})$$

where $\Xi_{i,n}$ and $\Theta_{i,n}^{(-)}$ are new frequency amplitudes that must be determined in terms of $\Theta_{i,n}$, h and $K^{(-)}$. The lower layer wavenumber $k_n^{(-)}$ is analogous to k_n , as defined in Eq. (23), where

$$k_n^{(-)} = \left(\frac{i\rho C_p \omega n}{K^{(-)}} \right)^{1/2}, \quad \text{with } \text{Re}(k_n^{(-)}) > 0. \quad (\text{C13})$$

The thermal solution form of Eq. (C12) is entirely analogous to Eq. (22). The solution for the lowest layer is designed to have zero flux as $z \rightarrow -\infty$. The solutions across the layer separation $z = -h$ are connected to one another for each value of n by imposing the continuity of temperature across the level, i.e.,

$$\Theta_{i,n} e^{-k_n h} + \Xi_{i,n} e^{k_n h} = \Theta_{i,n}^{(-)}, \quad (\text{C14})$$

as well as the continuity of thermal flux across the layer, i.e.

$$\left[K \partial_z T \right]_{z \rightarrow -h^-}^{z \rightarrow -h^+} = 0, \quad (\text{C15})$$

which means that for each index n we require

$$k_n \Theta_{i,n} e^{-k_n h} - k_n \Xi_{i,n} e^{k_n h} = k_n^{(-)} \Theta_{i,n}^{(-)}. \quad (\text{C16})$$

Solving these two simultaneous equations admits

$$\Xi_{i,n} = \Theta_{i,n} \frac{1 - \sqrt{K/K^{(-)}}}{1 + \sqrt{K/K^{(-)}}} e^{-2hk_n}, \quad \Theta_{i,n}^{(-)} = \frac{2\Theta_{i,n} e^{-hk_n}}{1 + \sqrt{K/K^{(-)}}}. \quad (\text{C17})$$

Therefore, the temperature at the surface is

$$T_i = \sum_{n=0}^N \Theta_{i,n} \left(1 + \frac{1 - \sqrt{K/K^{(-)}}}{1 + \sqrt{K/K^{(-)}}} e^{-2hk_n} \right) e^{-i\omega n t} + \text{c.c.}, \quad (\text{C18})$$

while the conductive flux is

$$\Lambda_i = K \partial_z T_i = \sum_{n=1}^N k_n \Theta_{i,n} \left(1 - \frac{1 - \sqrt{K/K^{(-)}}}{1 + \sqrt{K/K^{(-)}}} e^{-2hk_n} \right) e^{-i\omega n t} + \text{c.c.} \quad (\text{C19})$$

Consequently, the solution method described in Sec. 3.4 may be executed exactly as it is there described, except for replacing Eq. (24) with Eq. (C19), and the surface temperature T_i replaced by the expression in Eq. (C18). In reference to the illustrative case described in Appendix B, Eq. (B11) would be rewritten instead as

$$F_n(\Theta_m) + K k_n \Theta_n \left(1 - \frac{1 - \sqrt{K/K^{(-)}}}{1 + \sqrt{K/K^{(-)}}} e^{-2hk_n} \right) - f_n = 0, \quad k_0 = 0. \quad (\text{C20})$$

The solution method described here may be straightforwardly generalized to multiple layers. The coefficients may be calculated using any symbolic mathematics software or using any prepackaged linear system solver.

D. SUBSURFACE RADIATIVE TRANSFER DETAILS

In order to connect these interior thermal solutions to the observed brightness temperature, $T_{b,\text{obs}} = 29 \pm 5\text{K}$, measured by New Horizons REX instrument, we have implemented the radiative transfer calculation detailed at length in de Kleer et al. (2021). A brightness temperature T_b is defined as the temperature of a blackbody that produces the observed radiative intensity at frequency ν . We designate the Arrokoth disk averaged REX observed intensity by $I(\text{REX})$, which is the sum of the disk-averaged Arrokoth emitted intensity at frequency ν (\tilde{I}_ν) plus the intensity received from the cosmic microwave background ($I_{\nu,\text{cmb}}$). The identification between $I(\text{REX})$ and $T_{b,\text{obs}}$ comes from the solution of

$$I(\text{REX}) = \tilde{I}_\nu + I_{\nu,\text{cmb}} = \frac{2h\nu^3/c^2}{\exp\left[\frac{h\nu}{kT_{b,\text{obs}}}\right] - 1} + \frac{2h\nu^3/c^2}{\exp\left[\frac{h\nu}{kT_{\text{cmb}}}\right] - 1}, \quad (\text{D21})$$

where h is Planck's constant, c speed of light and where the frequency $\nu = c/\lambda$. Given that the X-band REX observation occurs at a wavelength $\lambda = 0.04\text{m}$, places this emission in the Rayleigh-Jeans end of the blackbody spectrum as $T_\nu \equiv h\nu/k \approx 0.36\text{K} \ll T_{b,\text{obs}}$ and T_{cmb} , which simplifies the above into

$$I(\text{REX}) = \frac{2k\nu^2}{c^2} (T_{b,\text{obs}} + T_{\text{cmb}}). \quad (\text{D22})$$

\tilde{I}_ν is the average of the emitted intensity ($\tilde{I}_{\nu,i}$) across the set of all spacecraft-viewable facets i weighted by each facet's spacecraft projected area σ_i . We do not include any Gaussian weighting that would take into account of the

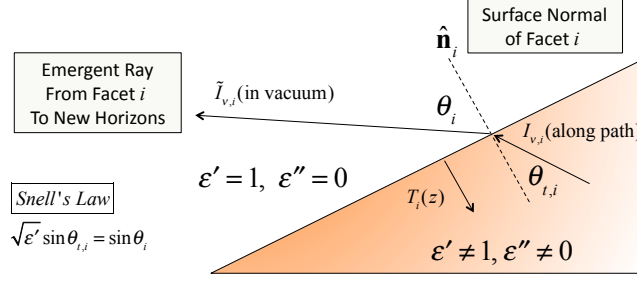


Figure 23. Diagram for simple radiative transfer calculation.

REX beam. For each facet i with unit normal vector $\hat{\mathbf{n}}_i$ we define θ_i as the emission angle of the rays emitted from the surface that reach the spacecraft, from which it follows that if each facet has total area s_i , then $\sigma_i = s_i \cos \theta_i$. For geometrical reference see both Fig. 23 as well as Fig. 22 in Appendix A. By construction it follows that

$$\tilde{I}_\nu = \frac{\sum_{\forall i \text{ visible}} \tilde{I}_{\nu,i} \sigma_i}{\sum_{\forall i \text{ visible}} \sigma_i}, \quad (\text{D23})$$

where all facets viewable by the spacecraft at the time of observations is derived directly from the network analysis that went into developing Arrokoth's thermal solutions as described in Section 3 and Appendix A.

The intensity $\tilde{I}_{\nu,i}$ emerging from the surface is the resulting radiation as having propagated from the interior. This radiation originates from all points beneath the surface as attenuated on a scale set by the electric skin depth δ_{elec} , where

$$\delta_{\text{elec}} \equiv \frac{\lambda}{4\pi\kappa}, \quad (\text{D24})$$

in which $\kappa = \text{Im}(n)$ and where n is the complex index of refraction of the medium that is related to the dielectric constant ϵ via $\epsilon \equiv n^2$, and is generally a function of a photon's wavelength. While the electric skin depth is temperature dependent, for simplicity hereafter we will treat it as insensitive to temperature. A material's ϵ is usually measured in the laboratory (e.g., for cometary ices at radar wavelengths see Heggy et al. 2012) and is tabulated in terms of its real and imaginary parts for which we use the convention in de Kleer et al. (2021), $\epsilon' \equiv \text{Re}(\epsilon)$ and $\epsilon'' \equiv \text{Im}(\epsilon)$. In all of our calculations below, we assume that ϵ has no subsurface variation. As such

$$\tilde{I}_{\nu,i}(\cos \theta_i) = \frac{\langle E_{\text{eff}} \rangle \int_0^\infty I_{\nu,i}(z) e^{-z/(\delta_{\text{elec}} \cos \theta_{t,i})} dz}{\int_0^\infty e^{-z/(\delta_{\text{elec}} \cos \theta_{t,i})} dz} \quad (\text{D25})$$

where z is depth as measured normal to facet i 's surface, $\theta_{t,i}$ is the angle formed between a subsurface propagating photon's path and facet i 's unit normal (for reference see Fig. 23). We have formally included an X-band emissivity factor $\langle E_{\text{eff}} \rangle$ as is common practice when dealing with solar system ices of unknown structural and transmission properties. Because we have assumed ϵ is constant in the subsurface the photon's subsurface slant-path trajectory changes upon exiting into vacuum and, therefore, $\theta_{t,i}$ relates to θ_i via Snell's Law, which following its reformulation in de Kleer et al. (2021), is given by

$$\cos \theta_{t,i} = \sqrt{1 - \frac{\sin^2 \theta_i}{\epsilon'}}. \quad (\text{D26})$$

The subsurface intensity $I_{\nu,i}$ is

$$I_{\nu,i}(z) = \frac{2h\nu^3/c^2}{\exp\left[\frac{h\nu}{kT_i(z)}\right] - 1} \approx \frac{2k\nu^2}{c^2} T_i(z), \quad (\text{D27})$$

The Rayleigh-Jeans limit is the approximate form given on the RHS of Eq. (D27). The subsurface temperature profile beneath facet i , $T_i = T_i(z, \mathcal{I}, \dots)$, are those as determined in previous sections, and we note that these temperature solutions depends upon the material's thermal inertia (\mathcal{I}), which we shall keep general for our considerations forthwith.

Using the Rayleigh-Jeans limiting form of Eq. (D27) in (D25) permits the re-expression of Eq. (D23) in terms of a model prediction brightness temperature, hereafter simply as T_b ,

$$\tilde{I}_\nu = \frac{2k\nu^2}{c^2} T_b(\mathcal{I}, \varepsilon', \varepsilon'', \langle E_{\text{eff}} \rangle), \quad (\text{D28})$$

where

$$T_b = T_b(\mathcal{I}, \varepsilon', \varepsilon'', \langle E_{\text{eff}} \rangle) = \overline{T}_{b,i} \equiv \frac{\sum_{\forall i \text{ visible}} \sigma_i T_{b,i}}{\sum_{\forall i \text{ visible}} \sigma_i}, \quad (\text{D29})$$

with a predicted X-band brightness temperature for each visible facet i , $T_{b,i}$ defined by

$$T_{b,i}(\mathcal{I}, \varepsilon', \varepsilon'', \langle E_{\text{eff}} \rangle) \equiv \frac{\langle E_{\text{eff}} \rangle \int_0^\infty T_i(z, \mathcal{I}) e^{-z/(\delta_{\text{elec}} \cos \theta_{t,i})} dz}{\delta_{\text{elec}} \cos \theta_{t,i}}. \quad (\text{D30})$$

The overline symbol is intended here as a short-hand representation of the facet-area weighted averaging. For any given instantaneous temperature solution determined using the methods of section 3, we can produce a model prediction T_b that can be compared directly against the REX observed value $T_{b,\text{obs}}$. T_b is a function of four unknown parameters, i.e., \mathcal{I} (through T_i), the real and imaginary parts of the dielectric constant ϵ , and the X-band emissivity $\langle E_{\text{eff}} \rangle$. The dielectric constant determines the electric skin depth (δ_{elec}) and the photon's subsurface propagation angle $\theta_{t,i}$ that leads to a photon emission angle θ_i that, upon leaving Arrokoth's surface, leads directly to the spacecraft. Each $\theta_{t,i}$ is calculated by Snell's Law, Eq. (D26), which is a known function of the set of viewing angles θ_i formed between each facet's unit normal $\hat{\mathbf{n}}_i$ and the line connecting the spacecraft's position to each facet's center.

We note that using an averaging approach Bird et al. (2022) develop T_b along a parallel route that short-circuits the large scale computations involved in developing Eq. (D29) from Eq. (D30). Instead, T_b is estimated straight away from (D30) where T_i is replaced by a visible facet surface area weighted temperature, $\overline{T_i(z)}$, and $\theta_{t,i}$ is replaced with a similarly facet area weighted average of the spacecraft-surface-normal inclination angle, $\overline{\theta_t}$. In other words

$$T_b \approx \frac{\langle E_{\text{eff}} \rangle \int_0^\infty \overline{T_i(z, \mathcal{I})} e^{-z/(\delta_{\text{elec}} \cos \overline{\theta_{t,i}})} dz}{\delta_{\text{elec}} \cos \overline{\theta_{t,i}}}. \quad (\text{D31})$$

Formally speaking, the two approaches are not-commensurate as the average of products – namely that of the temperature and the depth dependent exponential factor – is not necessarily equal to the product of their averages. However, we do find that in this application the final results are largely consistent with one another.

Thus, Following the procedures described in Section 3, we construct a set of model temperature solutions for several values of \mathcal{I}_j contained in the range of 0.5tiu and 300tiu. We collect the set of predicted temperature solutions for encounter day $T_i(z, \mathcal{I}_j)$ and generate predicted values of T_b for the range of dielectric values $1 < \varepsilon' < 3.5$ and $10^{-4} < \varepsilon'' < 10$, which are motivated by those values of ϵ thought to be relevant to cometary ices. The numerical solutions determined for each $T_i(z, \mathcal{I}_j)$ are tabulated only down to a depth $z_b = 10\text{m}$ because we find that the temperatures below that depth have asymptoted to their orbitally averaged values, i.e., $T_i(z > z_b, \mathcal{I}_j) \approx T_i(z_b, \mathcal{I}_j)$. As such, the integral in Eq. (D30) is well-approximated with

$$\frac{\int_0^\infty T_i(z, \mathcal{I}_j) e^{-z/(\delta_{\text{elec}} \cos \theta_{t,i})} dz}{\delta_{\text{elec}} \cos \theta_{t,i}} \approx \frac{\int_0^{z_b} T_i(z, \mathcal{I}_j) e^{-z/(\delta_{\text{elec}} \cos \theta_{t,i})} dz}{\delta_{\text{elec}} \cos \theta_{t,i}} + T_i(z_b, \mathcal{I}_j) e^{-z_b/(\delta_{\text{elec}} \cos \theta_{t,i})}. \quad (\text{D32})$$

We observe that the added correction term on the RHS of the above expression is important only when $\delta_{\text{elec}} \cos \theta_{t,i} \ll z_b$.

Fig. 15 displays predicted T_b for eight selected values of \mathcal{I} . Each color contour plot shows T_b as a function of ε' and ε'' . Drawn atop each are black contour lines representing $T_{b,\text{obs}} = 29\text{K}$, with dashed black contours showing

the error bounds at 34K and 24K. Also drawn with white contours a level sets for four corresponding values of $\delta_{\text{elec}} = 10^{-2}, 10^{-1}, 1, 10\text{m}$, nominally indicating corresponding depths from which the bulk of the radiation emerges for a given value of ε of interest. The qualities and implications of these solutions are discussed further in the body of the text. However we do observe from Fig. 15 that the predicted values of T_b are weakly dependent on ε' in the range 1 and 3.5.

REFERENCES

- Andersson, O., & Suga, H. 1994, *Solid State Communications*, 91, 985, doi: [10.1016/0038-1098\(94\)90438-3](https://doi.org/10.1016/0038-1098(94)90438-3)
- Attree, N., Groussin, O., Jorda, L., et al. 2018, *A&A*, 610, A76, doi: [10.1051/0004-6361/201731937](https://doi.org/10.1051/0004-6361/201731937)
- Beyer, R., Porter, S., Schenk, P., et al. 2019a, in *EPSC-DPS Joint Meeting 2019*, Vol. 2019, EPSC-DPS2019-849
- Beyer, R. A., Weaver, H. A., Porter, S. B., et al. 2019b, in *Lunar and Planetary Science Conference, Lunar and Planetary Science Conference*, 2258
- Bierson, C. J., & Nimmo, F. 2019, *Icarus*, 326, 10, doi: [10.1016/j.icarus.2019.01.027](https://doi.org/10.1016/j.icarus.2019.01.027)
- Brouet, Y., Levasseur-Regourd, A. C., Sabouroux, P., et al. 2015, *A&A*, 583, A39, doi: [10.1051/0004-6361/201526099](https://doi.org/10.1051/0004-6361/201526099)
- Buie, M. W., Porter, S. B., Tamblyn, P., et al. 2020, *AJ*, 159, 130, doi: [10.3847/1538-3881/ab6ced](https://doi.org/10.3847/1538-3881/ab6ced)
- Castillo-Rogez, J., Vernazza, P., & Walsh, K. 2019, *MNRAS*, 486, 538, doi: [10.1093/mnras/stz786](https://doi.org/10.1093/mnras/stz786)
- Castillo-Rogez, J. C., Johnson, T. V., Thomas, P. C., et al. 2012, *Icarus*, 219, 86, doi: [10.1016/j.icarus.2012.02.002](https://doi.org/10.1016/j.icarus.2012.02.002)
- Cruikshank, D. P., Imanaka, H., & Dalle Ore, C. M. 2005a, *Advances in Space Research*, 36, 178, doi: [10.1016/j.asr.2005.07.026](https://doi.org/10.1016/j.asr.2005.07.026)
- Cruikshank, D. P., Owen, T. C., Dalle Ore, C., et al. 2005b, *Icarus*, 175, 268, doi: [10.1016/j.icarus.2004.09.003](https://doi.org/10.1016/j.icarus.2004.09.003)
- de Kleer, K., Butler, B., de Pater, I., et al. 2021, *PSJ*, 2, 5, doi: [10.3847/PSJ/abcbf4](https://doi.org/10.3847/PSJ/abcbf4)
- Earle, A. M., Binzel, R. P., Young, L. A., et al. 2017, *Icarus*, 287, 37, doi: [10.1016/j.icarus.2016.09.036](https://doi.org/10.1016/j.icarus.2016.09.036)
- Efimov, V. B., Izotov, A. N., Levchenko, A. A., Mezhov-Deglin, L. P., & Khasanov, S. S. 2011, *JETP Letters*, 94, 621
- Estrada, P. R., Cuzzi, J. N., & Morgan, D. A. 2016, *ApJ*, 818, 200, doi: [10.3847/0004-637X/818/2/200](https://doi.org/10.3847/0004-637X/818/2/200)
- Ferrari, C. 2018, *SSRv*, 214, 111, doi: [10.1007/s11214-018-0546-x](https://doi.org/10.1007/s11214-018-0546-x)
- Ferrari, C., & Lucas, A. 2016, *A&A*, 588, A133, doi: [10.1051/0004-6361/201527625](https://doi.org/10.1051/0004-6361/201527625)
- Ferrari, C., Lucas, A., & Jacquemoud, S. 2021, *A&A*, 655, A8, doi: [10.1051/0004-6361/202141223](https://doi.org/10.1051/0004-6361/202141223)
- Flasar, F. M., Achterberg, R. K., Conrath, B. J., et al. 2005, *Science*, 307, 1247, doi: [10.1126/science.1105806](https://doi.org/10.1126/science.1105806)
- Fray, N., & Schmitt, B. 2009, *Planet. Space Sci.*, 57, 2053, doi: [10.1016/j.pss.2009.09.011](https://doi.org/10.1016/j.pss.2009.09.011)
- Gläser, P., & Gläser, D. 2019, *A&A*, 627, A129, doi: [10.1051/0004-6361/201935514](https://doi.org/10.1051/0004-6361/201935514)
- Grundy, W. M., Binzel, R. P., Buratti, B. J., et al. 2016, *Science*, 351, aad9189, doi: [10.1126/science.aad9189](https://doi.org/10.1126/science.aad9189)
- Grundy, W. M., Bird, M. K., Britt, D. T., et al. 2020, *Science*, 367, aay3705, doi: [10.1126/science.aay3705](https://doi.org/10.1126/science.aay3705)
- Gundlach, B., & Blum, J. 2012, *Icarus*, 219, 618, doi: [10.1016/j.icarus.2012.03.013](https://doi.org/10.1016/j.icarus.2012.03.013)
- Gusarov, A., Laoui, T., Froyen, L., & Titov, V. 2003, *Int. J. Heat Mass Transfer*, 46, 1103, doi: [10.1016/S0017-9310\(02\)00370-8](https://doi.org/10.1016/S0017-9310(02)00370-8)
- Hartmann, W. K. 1987, *Icarus*, 71, 57, doi: [10.1016/0019-1035\(87\)90162-X](https://doi.org/10.1016/0019-1035(87)90162-X)
- Heggy, E., Palmer, E. M., Kofman, W., et al. 2012, *Icarus*, 221, 925, doi: [10.1016/j.icarus.2012.09.023](https://doi.org/10.1016/j.icarus.2012.09.023)
- Hofgartner, J. D., Buratti, B. J., Benecchi, S. D., et al. 2021, *Icarus*, 356, 113723, doi: [10.1016/j.icarus.2020.113723](https://doi.org/10.1016/j.icarus.2020.113723)
- Howett, C. J. A., Spencer, J. R., Pearl, J., & Segura, M. 2010, *Icarus*, 206, 573, doi: [10.1016/j.icarus.2009.07.016](https://doi.org/10.1016/j.icarus.2009.07.016)
- Hu, X., Shi, X., Sierks, H., et al. 2017, *MNRAS*, 469, S295, doi: [10.1093/mnras/stx1607](https://doi.org/10.1093/mnras/stx1607)
- Jackson, A. P., & Desch, S. J. 2021, *Journal of Geophysical Research (Planets)*, 126, e06706, doi: [10.1029/2020JE006706](https://doi.org/10.1029/2020JE006706)
- Jagota, A., Paretkar, D., & Ghatak, A. 2012, *PhRvE*, 85, 051602, doi: [10.1103/PhysRevE.85.051602](https://doi.org/10.1103/PhysRevE.85.051602)
- Johnson, K. L., Kendall, K., & Roberts, A. D. 1971, *Proceedings of the Royal Society of London Series A*, 324, 301, doi: [10.1098/rspa.1971.0141](https://doi.org/10.1098/rspa.1971.0141)
- Johnson, T. V., & Lumine, J. I. 2005, *Nature*, 435, 69, doi: [10.1038/nature03384](https://doi.org/10.1038/nature03384)
- Keane, J. T., Umurhan, O. M., Porter, S. B., et al. 2020, in *Lunar and Planetary Science Conference, Lunar and Planetary Science Conference*, 2444
- Klinger, J. 1980, *Science*, 209, 271, doi: [10.1126/science.209.4453.271](https://doi.org/10.1126/science.209.4453.271)
- Le Gall, A., Leyrat, C., Janssen, M. A., et al. 2014, *Icarus*, 241, 221, doi: [10.1016/j.icarus.2014.06.011](https://doi.org/10.1016/j.icarus.2014.06.011)

- Le Gall, A., Malaska, M. J., Lorenz, R. D., et al. 2016, *Journal of Geophysical Research (Planets)*, 121, 233, doi: [10.1002/2015JE004920](https://doi.org/10.1002/2015JE004920)
- Lebofsky, L. A. 1975, *Icarus*, 25, 205, doi: [10.1016/0019-1035\(75\)90020-2](https://doi.org/10.1016/0019-1035(75)90020-2)
- Lellouch, E., Santos-Sanz, P., Lacerda, P., et al. 2013, *A&A*, 557, A60, doi: [10.1051/0004-6361/201322047](https://doi.org/10.1051/0004-6361/201322047)
- Lisse, C. M., Young, L. A., Cruikshank, D. P., et al. 2021, *Icarus*, 356, 114072, doi: [10.1016/j.icarus.2020.114072](https://doi.org/10.1016/j.icarus.2020.114072)
- Matson, D. L., Castillo-Rogez, J. C., Schubert, G., Sotin, C., & McKinnon, W. B. 2009, *The Thermal Evolution and Internal Structure of Saturn's Mid-Sized Icy Satellites*, ed. M. K. Dougherty, L. W. Esposito, & S. M. Krimigis, 577, doi: [10.1007/978-1-4020-9217-6_18](https://doi.org/10.1007/978-1-4020-9217-6_18)
- McKinnon, W. B., Richardson, D. C., Marohnic, J. C., et al. 2020, *Science*, 367, aay6620, doi: [10.1126/science.aay6620](https://doi.org/10.1126/science.aay6620)
- Mellon, M. T. 1997, *J. Geophys. Res.*, 102, 25617, doi: [10.1029/97JE02582](https://doi.org/10.1029/97JE02582)
- Meyer, C. D., Balsara, D. S., & Aslam, T. D. 2012, *MNRAS*, 422, 2102, doi: [10.1111/j.1365-2966.2012.20744.x](https://doi.org/10.1111/j.1365-2966.2012.20744.x)
- Molaro, J. L., Byrne, S., & Langer, S. A. 2015, *Journal of Geophysical Research (Planets)*, 120, 255, doi: [10.1002/2014JE004729](https://doi.org/10.1002/2014JE004729)
- Müller, T., Lellouch, E., & Fornasier, S. 2020, in *The Trans-Neptunian Solar System*, ed. D. Prialnik, M. A. Barucci, & L. Young, 153–181, doi: [10.1016/B978-0-12-816490-7.00007-2](https://doi.org/10.1016/B978-0-12-816490-7.00007-2)
- Ostro, S. J., West, R. D., Janssen, M. A., et al. 2006, *Icarus*, 183, 479, doi: [10.1016/j.icarus.2006.02.019](https://doi.org/10.1016/j.icarus.2006.02.019)
- Paillou, P., Lunine, J., Ruffié, G., et al. 2008, *Geophys. Res. Lett.*, 35, L18202, doi: [10.1029/2008GL035216](https://doi.org/10.1029/2008GL035216)
- Pätzold, M., Andert, T., Hahn, M., et al. 2016, *Nature*, 530, 63, doi: [10.1038/nature16535](https://doi.org/10.1038/nature16535)
- Piqueux, S., & Christensen, P. R. 2009, *Journal of Geophysical Research (Planets)*, 114, E09005, doi: [10.1029/2008JE003308](https://doi.org/10.1029/2008JE003308)
- Porter, S., Beyer, R., Keane, J., et al. 2019, in *EPSC-DPS Joint Meeting 2019*, Vol. 2019, EPSC–DPS2019–311
- Porter, S. B., Buie, M. W., Parker, A. H., et al. 2018, *AJ*, 156, 20, doi: [10.3847/1538-3881/aac2e1](https://doi.org/10.3847/1538-3881/aac2e1)
- Richardson, J. E., & Bowling, T. J. 2014, *Icarus*, 234, 53, doi: [10.1016/j.icarus.2014.02.015](https://doi.org/10.1016/j.icarus.2014.02.015)
- Richardson, J. E., Graves, K. J., Harris, A. W., & Bowling, T. J. 2019, *Icarus*, 329, 207, doi: [10.1016/j.icarus.2019.03.027](https://doi.org/10.1016/j.icarus.2019.03.027)
- Rivera-Valentin, E. G., Blackburn, D. G., & Ulrich, R. 2011, *Icarus*, 216, 347, doi: [10.1016/j.icarus.2011.09.006](https://doi.org/10.1016/j.icarus.2011.09.006)
- Rozitis, B., & Green, S. F. 2011, *MNRAS*, 415, 2042, doi: [10.1111/j.1365-2966.2011.18718.x](https://doi.org/10.1111/j.1365-2966.2011.18718.x)
- Schloerb, F. P., Keilm, S., von Allmen, P., et al. 2015, *A&A*, 583, A29, doi: [10.1051/0004-6361/201526152](https://doi.org/10.1051/0004-6361/201526152)
- Schmitt, B., Philippe, S., Grundy, W. M., et al. 2017, *Icarus*, 287, 229, doi: [10.1016/j.icarus.2016.12.025](https://doi.org/10.1016/j.icarus.2016.12.025)
- Shoshany, Y., Prialnik, D., & Podolak, M. 2002, *Icarus*, 157, 219, doi: [10.1006/icar.2002.6815](https://doi.org/10.1006/icar.2002.6815)
- Shulman, L. M. 2004, *A&A*, 416, 187, doi: [10.1051/0004-6361:20031746](https://doi.org/10.1051/0004-6361:20031746)
- Simon, J. I., Cuzzi, J. N., McCain, K. A., et al. 2018, *Earth and Planetary Science Letters*, 494, 69, doi: [10.1016/j.epsl.2018.04.021](https://doi.org/10.1016/j.epsl.2018.04.021)
- Spencer, J. R., Pearl, J. C., Segura, M., & Cassini CIRS. 2004, in *AAS/Division for Planetary Sciences Meeting Abstracts*, Vol. 36, AAS/Division for Planetary Sciences Meeting Abstracts #36, 04.07
- Spencer, J. R., Stern, S. A., Moore, J. M., et al. 2020, *Science*, 367, aay3999, doi: [10.1126/science.aay3999](https://doi.org/10.1126/science.aay3999)
- Stern, S. A., Keeney, B., Singer, K. N., et al. 2021, *PSJ*, 2, 87, doi: [10.3847/PSJ/abee26](https://doi.org/10.3847/PSJ/abee26)
- Stern, S. A., Weaver, H. A., Spencer, J. R., et al. 2019, *Science*, 364, aaw9771, doi: [10.1126/science.aaw9771](https://doi.org/10.1126/science.aaw9771)
- Style, R. W., Boltyanskiy, R., Che, Y., et al. 2013, *PhRvL*, 110, 066103, doi: [10.1103/PhysRevLett.110.066103](https://doi.org/10.1103/PhysRevLett.110.066103)
- Titus, T. N., & Cushing, G. E. 2012, in *Third International Planetary Dunes Workshop: Remote Sensing and Data Analysis of Planetary Dunes*, Vol. 1673, 95–96
- Tosi, F., Capaccioni, F., Capria, M. T., et al. 2019, *Nature Astronomy*, 3, 649, doi: [10.1038/s41550-019-0740-0](https://doi.org/10.1038/s41550-019-0740-0)
- Umurhan, O. M., Keane, J. T., Porter, S. B., et al. 2019, in *EPSC-DPS Joint Meeting 2019*, Vol. 2019, EPSC–DPS2019–749
- Verbiscer, A. J., Skrutskie, M. F., & Hamilton, D. P. 2009, *Nature*, 461, 1098, doi: [10.1038/nature08515](https://doi.org/10.1038/nature08515)
- White, O. L., Umurhan, O. M., Moore, J. M., & Howard, A. D. 2016, *Journal of Geophysical Research (Planets)*, 121, 21, doi: [10.1002/2015JE004846](https://doi.org/10.1002/2015JE004846)